



**HAL**  
open science

## A well-resolved numerical study of a turbulent buoyant helium jet in a highly-confined two-vented enclosure

Elie Saikali, Anne Sergent, Yanshu Wang, Patrick Le Quéré, Gilles Bernard-Michel, Christian Tenaud

### ► To cite this version:

Elie Saikali, Anne Sergent, Yanshu Wang, Patrick Le Quéré, Gilles Bernard-Michel, et al.. A well-resolved numerical study of a turbulent buoyant helium jet in a highly-confined two-vented enclosure. *International Journal of Heat and Mass Transfer*, 2020, 163, pp.120470:1-20. 10.1016/j.ijheatmasstransfer.2020.120470 . hal-02998143

**HAL Id: hal-02998143**

**<https://hal.science/hal-02998143>**

Submitted on 27 Nov 2020

**HAL** is a multi-disciplinary open access archive for the deposit and dissemination of scientific research documents, whether they are published or not. The documents may come from teaching and research institutions in France or abroad, or from public or private research centers.

L'archive ouverte pluridisciplinaire **HAL**, est destinée au dépôt et à la diffusion de documents scientifiques de niveau recherche, publiés ou non, émanant des établissements d'enseignement et de recherche français ou étrangers, des laboratoires publics ou privés.

# A well-resolved numerical study of a turbulent buoyant helium jet in a highly-confined two-vented enclosure

Elie Saikali<sup>1,2</sup>, Anne Sergent<sup>1,3,\*</sup>, Yanshu Wang<sup>1,2</sup>, Patrick Le Quéré<sup>1</sup>, Gilles Bernard-Michel<sup>2</sup> and Christian Tenaud<sup>1</sup>

<sup>1</sup> *LIMSI-CNRS, Université Paris-Saclay, 91405 Orsay, France,*

<sup>2</sup> *DEN-STMF, CEA Paris-Saclay, 91191 Gif-Sur-Yvette cedex, France,*

<sup>3</sup> *Sorbonne Université, UFR 919 Ingénierie, 75005, Paris, France,*

\* *anne.sergent@limsi.fr*

---

## Abstract

A numerical study of a turbulent buoyant helium jet developing in a two-vented cavity is conducted based on a well-resolved numerical simulation. A sufficiently large exterior region is modelled in the computational domain to approach the natural inlet/outlet conditions of the vents, leading to a good agreement between the numerical results and available experimental particle image velocimetry (PIV) measurements. For a release of helium with a flow rate of 5 Nl/min in an air-filled cavity about 15 cm high, the flow structure and the helium dispersion are analysed illustrating the strong confinement effect enhanced by a cross-flow from the lower vent. By tracking the jet axis deviation and comparing the classic plume description in terms of global fluxes estimated from DNS results to the Morton et al.' theory [1], we quantify the effect of the confinement and the cross-flow on the flow structure. Finally, we highlight a blocking zone at mid-cavity height originated from confinement, where helium accumulates.

*Keywords:* convection; emptying-filling box ; air/helium mixture; turbulence; direct numerical simulations; hydrogen safety.

---

## 1. Introduction

Hydrogen possesses two main properties, a very large specific energy per unit mass while producing no CO<sub>2</sub> during combustion. These characteristics make it a promising energy carrier to help reduce emissions of greenhouse gases. Its deployment has however been hindered by safety considerations due to its very high flammability and/or explosion risks. Its large scale industrial or domestic deployment thus requires that tools be available to evaluate these risks at the design stage. It is therefore of utmost importance to be able to quantify the space and time distributions of concentrations of hydrogen following accidental releases. While it is generally admitted that this hazard is not likely to happen when the release takes place in the open environment owing to the strong buoyant dispersion, the risk is deemed to be present if the release takes place in an enclosure or in a strongly confined configuration or vented enclosure such as parking lots or large fuel cell cabinets [2]. Vented enclosures are the most difficult to investigate and analyze due to the complex interplay between the dynamics and mixing properties of a turbulent buoyant jet and the simultaneous entrainment flow or discharges from the apertures of the cavity. This work was thus undertaken to qualify the capability of numerical simulation to quantitatively predict the flow structure in a two-vented enclosure with a buoyant discharge of helium at the cavity floor. Helium is considered as the light discharged fluid to ensure the security of experimental investigations [3].

According to the classification by Turner [4], plumes and jets differ mainly in the force that dominates at the position where the light fluid is discharged. Plumes correspond to dom-

inant buoyancy, while jets refer to flows driven by momentum. Intermediate situations, flows driven by both momentum and buoyancy, are often referred to as buoyant-jets. In accordance with the classification by Turner, the flow regime can be furthermore characterized by the dimensionless Richardson number ( $Ri$ ) which compares the ratio of buoyant-to-inertial strengths at the discharge position. Pure plumes correspond to  $Ri$  much greater than unity, while pure jets correspond to values much smaller than unity [5]. This paper focuses on a frequent situation ie a buoyant-jet with  $Ri$  slightly less than unity. Such a flow is known to undergo a transition from an inertial-driven jet into a buoyancy-driven plume at a short distance above the discharge location [6].

Morton, Taylor and Turner introduced in 1956 the first theoretical study of plumes in infinite media [1]. Their model, usually referred to as the MTT model, is based on four of assumptions, a canonical round structure, Boussinesq approximation, self-similar solution and a constant entrainment coefficient hypothesis (defined as the ratio of the radial velocity at the buoyant-jet border to a characteristic vertical velocity and usually denoted by a constant parameter  $\alpha$ ) respectively. Ever since, the assumption of constant  $\alpha$  has been the subject of continuous investigations, mostly experimental [7]. Assuming a top-hat profile for the vertical velocity component, different experimental studies have shown that  $\alpha$  ranges from 0.05 in pure jets up to 0.16 in pure plumes [8]. Later experimental investigations by Abraham [9] and by List and Imberger [10] illustrated further issues on the hypothesis of constant  $\alpha$ . In conclusion, generalizing a unique value or formulation for the entrainment

## Nomenclature

$A^*$	effective vent opening surface	$\nu$	kinematic viscosity
$B$	buoyancy flux	$\rho$	density
$d$	diameter of the injection tube	$\tau$	viscous stress tensor
$D$	diffusion coefficient	$\Omega$	flux integration area
$H$	height of the cavity		
$M$	molar mass		
$\dot{M}$	momentum flux	<i>Abbreviations</i>	
$Ma$	Mach number	CFD	computational fluid dynamics
$N$	stratification frequency	DNS	direct numerical simulations
$p$	thermodynamic pressure	LES	large eddy simulations
$P$	hydrodynamic pressure	LMN	low Mach number
$Q_v$	volumetric flow-rate	MTT	Morton Taylor Turner
$Q$	volume flux	PIV	particle image velocimetry
$Re$	Reynolds number	RMS	root mean square
$Ri$	Richardson number		
$Sc$	Schmidt number	<i>Subscripts</i>	
$t$	time variable	amb	ambient fluid
$\mathbf{u} = (u_1, u_2, u_3)$	velocity field	e	environment outside the buoyant jet
$\mathbf{x} = (x, y, z)$	space variable	i	interface of the upper homogeneous layer
$X$	volume fraction	inj	injected fluid
$Y$	mass fraction	th	theoretical modelling
		0	at the injection
		1	helium
<i>Greek parameter</i>			
$\alpha$	entrainment coefficient	<i>Notations</i>	
$\delta$	cell size	$\langle \cdot \rangle_t$	time-averaged operator
$\delta t$	time step	$ \cdot _{\cdot}$	2D magnitude
$\epsilon$	turbulent dissipation	$\text{rms}\{\cdot\}_t$	RMS operator
$\eta$	Kolmogorov length scale	$(\cdot)'$	fluctuating field
$\lambda_B$	Batchelor length scale	$(\cdot)'^N$	normalized fluctuating field
$\mu$	dynamic viscosity		

coefficient remains an issue for the MTT theory.

In semi-confined enclosures, applicability of the MTT theory is questionable due to break down of self-similarity assumption when interactions between the buoyant-jet and the confinement take place. Linden et al. [11, 12] introduced theoretical models for buoyant-jet flows in one or two vented configurations, usually referred to as emptying-filling box models. Similar to the filling box theory of Baines and Turner [13], Linden et al. defined the filling mechanism in the vented domain. The emptying process due to the natural ventilation follows a Bernoulli's law. As in the MTT theory, the entrainment coefficient remains a key parameter of the Linden models and is often taken constant. Moreover, the Boussinesq approximation is assumed to be valid. The presence of two homogeneous concentration layers separated by a so-called interface is an *a priori* assumption. Experimentally, it has been shown that the hypothesis of a clear-cut interface level stands when the inflow inertia force is small with respect to the buoyancy force [14]. However, when the inlet flow rate increases, an intermediate stratified layer forms between the two homogeneous layers due to an increase of the mixing processes. It has been demonstrated that the finite thickness of this intermediate region increases with the interface altitude [15], but also with the inlet flow rate [14].

Applying the two-layer stratification model of Linden et al. in semi-confined buoyant jet flows allows the estimation of the interface height and the upper homogeneous layer mean concentration, at steady state. However, the experimental investi-

gations by Hunt and Holford [16, 17] illustrated the problematic of the Boussinesq approximation in this model. Indeed, in Linden's et al. model, owing to the use of the Boussinesq approximation, the interface height depends only on non-dimensional geometrical parameters, namely the vent areas, the height of the domain and the discharge coefficient of the vent  $c_d$  which is assumed constant. Hunt and Holford mainly criticized the use of constant  $c_d$  as it can lead to overestimate the outflow rate at the vent, and consequently to underestimate the top buoyant layer thickness. The work of Hunt and Holford was later extended by Vauquelin et al. [18] where the theoretical model of Linden is generalized to non-Boussinesq case by assuming a variable vent discharge coefficient  $c_d$ . However, the assumption of constant entrainment coefficient  $\alpha$  remains, that is a limitation for the pre-safety calculations.

In parallel to these theoretical studies, Computational Fluid Dynamics (CFD) approaches have been used to predict and analyze the buoyant-jet development in a semi-confined enclosures. Their main advantage is to avoid the above-mentioned difficulties encountered by the theoretical models. However, CFD approaches of vented enclosures are faced with a major difficulty namely the specification of appropriate boundary conditions at the vent. This is indeed a very challenging task due to the fact that there is some evidence that one can find both inward and outward flow through a given vent, as is the case in a vertical chimney [19]. One way to circumvent this problem is to consider an exterior computational domain, as was

done in Saikali et al. [20]. This study was performed in order to determine, by trial and error, the size of the exterior domain and appropriate boundary conditions in order to obtain satisfactory comparisons with experimental data from particle image velocimetry (PIV) measurements carried out at CEA Saclay (LIEFT) [21, 22]. To keep the computational costs reasonable, the study was performed using a LES model. Comparisons showed that the LES simulation were able to reproduce reasonably well the time averaged velocity fields and flow pattern. Also, a good agreement was found with PIV concerning the cross-flow effect, namely the inclination and the deformation of the buoyant-jet axis. However, the prediction of the fluctuation intensity in the vicinity of the discharge position and along the jet axis was not quite satisfactory [23]. This lead us to perform a well-resolved numerical simulation in order to provide reference values that could be used to validate further numerical modelling.

In this paper, we make use of the classic theoretical models (i.e. the MTT and Linden models) to point out the particularities of highly confined ventilated flow, even though they are far from their range of validity. The objective of the work is manifold. First, we aim at comparing numerical results and the MTT description of the plume development in order to highlight the main differences of the flow with the ideal case of buoyant jets in a free environment. This will help us to describe the buoyant jet development in terms of a series of horizontal layers, which are then characterized through the time-averaged and fluctuating flow quantities along the jet axis. Then, we take advantage of the full 3D knowledge of the helium concentration field to illustrate the large inhomogeneity of the helium distribution that might be missed by construction by global theoretical approaches of plume development (i.e. in terms of 1D buoyant flux). Finally, rough estimates of the upper homogeneous layer parameters using the Linden's model allows us to review the basic assumptions of the ventilation models in order to reveal the main specific features of the flow being studied.

The paper is organized as follows. The physical problem and the governing equations are summarized in section 2. Section 3 presents the numerical set-up and some methodological issues. Section 4 seeks to characterize the quality of the numerical simulation, by describing the general flow structure and by comparing it with PIV measurements. In section 5, the plume fluxes calculated from the MTT theory or estimated by simulation are compared, leading to a description of the plume development inside the cavity. Then, the 3D flow is depicted in section 6 along the jet axis, but also in terms of helium distribution, followed by a final discussion about the basic assumptions of the classic ventilation model of Linden et al. [11] with respect to the study test case. Finally, conclusions and future perspectives are drawn in section 7.

## 2. Physical problem and governing equations

The experimental set-up has been developed at CEA Saclay in the framework of hydrogen security in accidental release scenarios [20]. It consists of a cavity with two vents whose dimensions in the horizontal, span-wise and vertical directions

are  $W \times L \times H = 0.049 \times 0.05 \times 0.149 \text{ m}^3$ , respectively. The two vents, of identical dimensions equal to  $0.05 \times 0.029 \text{ m}^2$ , are located at the floor and ceiling of the cavity. Pure helium is injected at the floor center through a cylindrical pipe of diameter  $d = 0.01 \text{ m}$ . A schematic representation of the configuration can be found in figure 1.

Helium is injected at a constant volumetric flow-rate equal to  $Q_{v,0} = 5.458 \text{ l.min}^{-1}$  (equivalent to  $5 \text{ Nl.min}^{-1}$ ), corresponding to a maximum velocity at the injection  $u_{inj} \approx 2.3 \text{ m.s}^{-1}$ . The set-up is kept at constant temperature ( $= 25^\circ \text{ C}$  and atmospheric pressure  $P_{thm} = 10^5 \text{ Pa}$ ). For these conditions, the physical properties of both fluids are given in table 1. Note the significant density variation since the injected fluid is approximately 7 times lighter than the ambient. The injection Richardson and Reynolds numbers are respectively  $Ri_{inj} = g(\rho_{amb} - \rho_{inj})d/(\rho_{inj}u_{inj}^2) \approx 0.114$  and  $Re_{inj} = \rho_{inj}u_{inj}d/\mu_{inj} \approx 195$ . The injection Reynolds number  $Re_{inj}$  is small enough to predict a laminar jet developing close to the injection.

Fluid	Injected (species 1)	Ambient (species 2)
<b>Density</b> [kg.m <sup>-3</sup> ]	$\rho_{inj} = 0.16148$	$\rho_{amb} = 1.16864$
<b>Dynamic viscosity</b> [ $\times 10^{-5} \text{ kg.m}^{-1}.\text{s}^{-1}$ ]	$\mu_{inj} = 1.918$	$\mu_{amb} = 1.792$
<b>Molar mass</b> [ $\times 10^{-2} \text{ kg.mol}^{-1}$ ]	$M_{inj} = 0.4003$	$M_{amb} = 2.897$

Table 1: Working fluid physical properties with the isothermal and isobar assumptions:  $T = 25^\circ \text{ C}$  and  $P_{thm} = 10^5 \text{ Pa}$ .

The flow is governed by the conservation equations of mass, momentum and species. The equation of state for a binary gas mixture is used to relate the mixture's density with the species mass fractions [24]. The energy conservation equation is not required here as far as the isothermal and isobar conditions are valid.

Owing to the smallness of the Mach number ( $Ma = 7 \times 10^{-3} < 0.1$ ) together with the large ambient-to-injection density ratio ( $\rho_{amb}/\rho_{inj} \approx 7.24$ ), a low Mach number (LMN) approximation of the conservation equations is appropriate.

Pressure is thus split as the sum of a spatially uniform and constant thermodynamic pressure  $p$  and a hydrodynamic pressure  $P(\mathbf{x}, t)$  dependent on both space and time [25].

The dimensional system of governing equations under the LMN approximation thus reads

$$\frac{\partial \rho}{\partial t} + \frac{\partial}{\partial x_i}(\rho u_i) = 0, \quad (1)$$

$$\frac{\partial \rho u_j}{\partial t} + \frac{\partial}{\partial x_i}(\rho u_j u_i) = -\frac{\partial P^*}{\partial x_j} + \frac{\partial \tau_{ij}}{\partial x_i} + \rho g_j, \quad (2)$$

$$\frac{\partial \rho Y_1}{\partial t} + \frac{\partial}{\partial x_i}(\rho Y_1 u_i) = \frac{\partial}{\partial x_i} \left( D \rho \frac{\partial Y_1}{\partial x_i} \right), \quad (3)$$

$$\rho = \frac{p}{RT} \left( \frac{Y_1}{M_{inj}} + \frac{Y_2}{M_{amb}} \right)^{-1}. \quad (4)$$

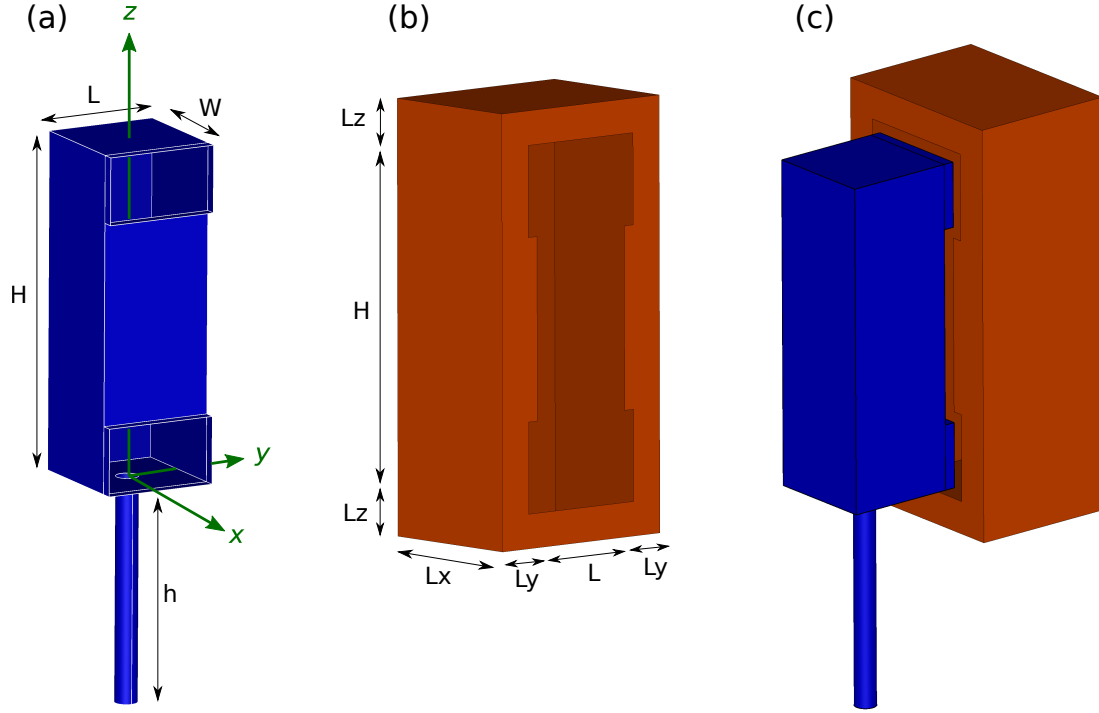


Figure 1: 3D view of the computational domain exhibiting the dimensions, the boundary conditions and the Cartesian orientation. Blue surfaces depict the position of the wall boundaries while red for open boundaries. (a) the studied cavity, (b) the exterior region, (c) the complete computational domain.

Here, the mixture density is  $\rho$ , while  $Y_1$  and  $Y_2$  denote respectively the helium (index 1) and air (index 2) mass fractions and satisfy the unity summation;  $Y_1 + Y_2 = 1$ .  $u_i$  is the mass weighted component in the  $i$ -direction of the velocity vector  $\mathbf{u} = (u_1, u_2, u_3)$ . We denote by  $\mathbf{g} = (0, 0, -g)$  the acceleration vector of the gravity.

The mixture diffusion coefficient is considered to be uniform and constant in the present work;  $D = 6.91 \times 10^{-5} \text{ m}^2 \cdot \text{s}^{-1}$ .  $R = 8.314 \text{ J} \cdot \text{K}^{-1} \cdot \text{mol}^{-1}$  denotes the classical specific gas constant and  $M$  the molar mass (see table 1). The viscous stress tensor for Newtonian fluids reads as  $\tau_{ij} = \mu(\partial u_j / \partial x_i + \partial u_i / \partial x_j)$ , with a pressure term defined as  $P^* = P + \frac{2}{3} \mu \partial u_k / \partial x_k$ .  $\mu$  denotes the dynamic viscosity defined for a binary gas mixture using the Wilke's gas mixture viscosity formula [26] as follows

$$\mu = \frac{Y_1 \mu_1}{Y_1 \phi_{11} + Y_2 \phi_{12}} + \frac{Y_2 \mu_2}{Y_1 \phi_{21} + Y_2 \phi_{22}}, \quad (5)$$

where  $\phi_{ij}$  is a set of dimensionless constants calculated as

$$\phi_{ij} = \frac{\frac{M_i}{M_j} \left[ 1 + \left( \frac{\mu_i}{\mu_j} \right)^{1/2} \left( \frac{M_j}{M_i} \right)^{1/4} \right]^2}{\left[ 8 \left( 1 + \frac{M_i}{M_j} \right) \right]^{1/2}} \quad ; \quad i, j = \{1, 2\}. \quad (6)$$

In what follows, the helium concentration is mostly expressed in terms of volume fraction  $X_1$ . The relationship between the mass and the volume fractions reads as

$$X_1 = (\rho - \rho_{\text{amb}}) / (\rho_{\text{inj}} - \rho_{\text{amb}}) = \rho Y_1 / \rho_{\text{inj}}. \quad (7)$$

### 3. Numerical set-up

#### 3.1. The computational domain

The numerical configuration mimics the CEA experiment [20]. Unless otherwise defined, the dimensions are identical to those of the experimental cavity.

A pipe of height  $h = 0.1 \text{ m}$  is modeled to ensure a well developed Poiseuille profile at the injection location inside the cavity. An external region attached directly to the vent surfaces is used to push the system boundary conditions away from the vents. As shown in our previous work [20], and taking into account the physical parameters of the problem, a sufficiently large external domain, equivalent to three volumes of the region of interest, is chosen in order to obtain a flow and a mixture distribution independent of the computational domain.

The horizontal extension of the exterior region is  $L_x = 6.75 \times 10^{-2} \text{ m}$ , span-wise length is  $L + (2 \times L_y)$  and the height is  $H + (2 \times L_z)$ , with  $L_y = L_z = 2 \times 10^{-2} \text{ m}$ . We consider a solid layer with a width of  $5 \times 10^{-3} \text{ m}$  around both vents in order to model the presence of the plexi-glass (wall thickness) in the experiment. Figure 1 displays a 3D view of the computational domain and illustrates the axis orientation.

The mesh is uniform with size  $\delta = 7 \times 10^{-4} \text{ m}$  in every direction. The total mesh contains 4,427,588 cells (cubes) that are distributed over 80 MPI subdomains.

#### 3.2. The CFD software and initial/boundary conditions

The simulation is carried out by the open source code Tri-oCFD within the TRUST platform, developed at CEA in the

Nuclear Energy Division (DEN) [27]. The discretization employs a Finite Difference Volume (FDV) method on a staggered grid. Spatial derivatives are discretized by a second order centered scheme except for the convective term of the species equation (3) where a third order QUICK scheme is used to ensure the monotonicity preserving constraints. A semi-implicit scheme (viscous/diffusion implicit) is used where the time integration is treated by a second order Rational Runge-Kutta (RRK2) scheme [28]. The time step is dynamic and satisfies the convective CFL = 1 criterion. Linear systems resulting from the implicit treatment of the diffusion terms are solved by a conjugate gradient method (CGM) [29]. An incremental projection method is used to treat the pressure-velocity coupling. The elliptic Poisson equation is solved by an iterative symmetric successive over relaxation (SSOR) algorithm.

The prescribed boundary conditions are the following: At the inlet boundary situated at the bottom end of the pipe, a fixed convective mass flux equal to  $\rho_{inj}Q$  is imposed with flat profiles for  $\rho = \rho_{inj}$  and  $Y_1 = 1$ , whereas a parabolic profile is imposed for  $\mathbf{u}$  so that the velocity vector is oriented along the vertical  $z$ -direction. On the wall boundaries, a no-slip boundary condition is applied for  $\mathbf{u}$  with a homogeneous Neumann condition for all the scalars  $\rho$ ,  $Y_1$  and  $P$ . At the open boundaries, an ambient-equilibrium pressure  $P = -\rho_{amb}gz$  is imposed for a considered height  $z$  with a homogeneous Neumann condition for  $\mathbf{u}$ . A homogeneous Neumann condition is imposed on  $\rho$  and  $Y_1$  if the fluid leaves the domain. Dirichlet conditions  $\rho = \rho_{amb}$  and  $Y_1 = 0$  are imposed on parts where the flow enters the domain. In order to reduce the transitional time period of the simulation, the initial condition is one instantaneous solution of our previous LES simulation [23].

### 3.3. Physical time and statistical recordings

The equations were integrated over a physical time lapse of 144 seconds with a time step equal to ( $\delta t \approx 1.4 \times 10^{-4}$  s). Time averaged, time fluctuating and root mean square (rms) fields are noted respectively for a considered quantity  $\varphi(\mathbf{x}, t)$  as  $\langle \varphi(\mathbf{x}, t) \rangle_t$ ,  $\varphi'(\mathbf{x}, t)$  and  $\text{rms}\{\varphi(\mathbf{x}, t)\}_t$ . The normalized fluctuations are defined as

$$\varphi'^N = \text{rms}\{\varphi\}_t / \langle \varphi \rangle_t . \quad (8)$$

Once the transitional time period is ended, the statistical fields are computed from an accumulation at each time step. Statistics were computed over two independent time windows  $W_1 = [85, 124]$  and  $W_2 = [124, 144]$ , corresponding to 39 and 20 seconds of physical data respectively. We have verified that the statistics are independent of the window with an accuracy better than  $10^{-6}m.s^{-1}$  for the velocity magnitude for instance.

The following section is devoted to a description of the flow pattern and to validation versus PIV measurements.

## 4. Flow description and comparison with PIV measurements

### 4.1. Flow pattern

The flow pattern in the vertical mid-plane at  $y = 0$  is depicted by the time-averaged iso-contours of the helium density  $\langle \rho \rangle_t$  (figure 2-a) and that of the 2D velocity magnitude

$\langle |\mathbf{u}|_{XZ} \rangle_t$  (figure 2-b), with  $|\mathbf{u}|_{XZ} = (u_1^2 + u_3^2)^{1/2}$ . This figure illustrates the entrainment of fresh air through the bottom vent resulting from the helium injection. The heavy air inflow impacts the rising buoyant jet resulting in a deviation of its axis towards the left wall facing the vents. By the Coanda effect, the upward flow and the left wall then interact over a large part of the cavity height, resulting in the attachment of the light mixing plume to the wall. After the impact with the top ceiling, the flow separates in two directions: a first small part recirculates near the top left corner, while a second part leaves the cavity due to the buoyancy aspiration from the top vent. A small part also recirculates downwards near the top vent.

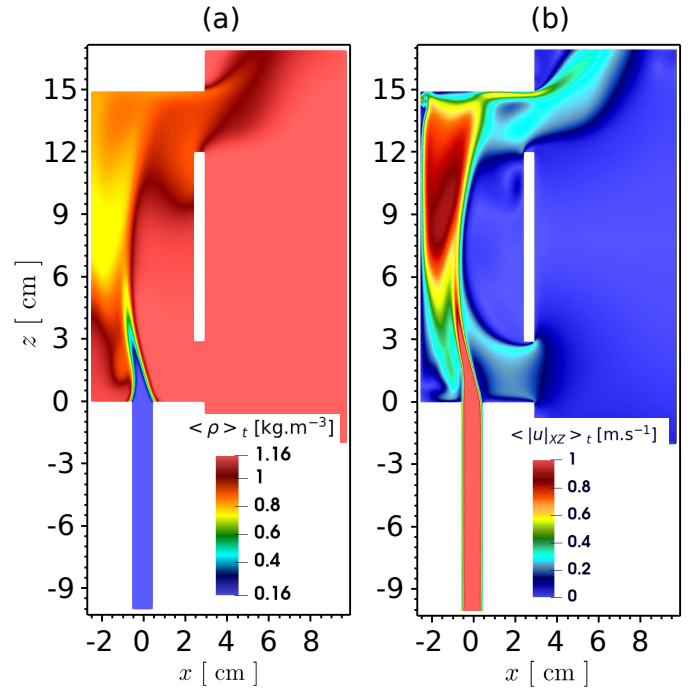


Figure 2: Iso-contours in the vertical mid-plane at  $y = 0$  illustrating the time-averaged flow pattern. (a) mixture density  $\langle \rho \rangle_t$ , (b) 2D velocity magnitude  $\langle |\mathbf{u}|_{XZ} \rangle_t$ .

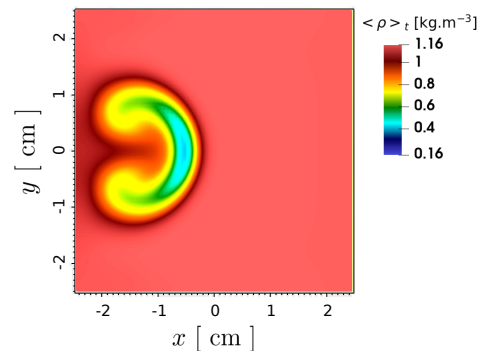


Figure 3: Iso-contours of helium density  $\langle \rho \rangle_t$  in the horizontal plane at  $z = 3$  cm illustrating the time-averaged cross-flow effect.

Figure 3 presents the iso-contours of  $\langle \rho \rangle_t$  in the horizontal plane through the top of the bottom vent at  $z = 3$  cm. This figure illustrates another aspect of the cross-flow effect

the crescent shape of the jet resulting from the formation of a counter-rotating vortex pair characteristic of the interaction of a jet and a cross flow [30].

#### 4.2. Turbulent length scales

In order to qualify the retained grid refinement, the resolved turbulent length scales are compared with the mesh size. From a dimensional analysis, a rough estimate of the Kolmogorov length scale  $\eta_{\text{DNS}}$  is defined as

$$\eta_{\text{DNS}} = \sqrt[4]{\frac{\langle \rho \rangle_t \langle \nu \rangle_t^3}{|\epsilon_{\text{DNS}}|}}, \quad (9)$$

where  $\nu$  is the kinematic viscosity of the mixture defined as  $\nu(\mathbf{x}, t) = \mu(\mathbf{x}, t)/\rho(\mathbf{x}, t)$  and  $\epsilon_{\text{DNS}}$  [ $\text{kg}\cdot\text{m}^{-1}\cdot\text{s}^{-3}$ ] denotes the turbulent dissipation term;

$$\epsilon_{\text{DNS}} = -\left\langle \tau'_{ik} \frac{\partial u'_i}{\partial x_k} \right\rangle_t. \quad (10)$$

Figure 4-a displays the ratio of the local mesh size  $\delta$  to the estimated  $\eta_{\text{DNS}}$  in the vertical mid-plane at  $y = 0$ . It is noted that the largest ratio values reach at most 3 and are mainly located at the top of the cavity where the plume impacts the ceiling, and near the left wall in the range of  $z \approx 5 - 7$  cm. Elsewhere, a ratio of unity or even smaller is recorded.

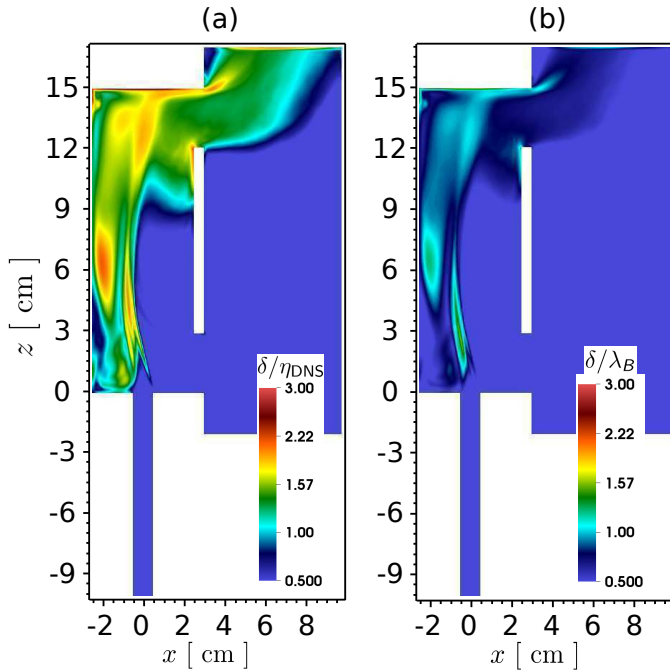


Figure 4: Iso-contours in the vertical mid-plane at  $y = 0$ . (a) ratio of the local grid size to the Kolmogorov length scale, (b) ratio of the local grid size to the Batchelor length scale.

As far as the species-mixing is also dependent on the employed mesh, we consider now the turbulent length scale of Batchelor  $\lambda_{B_{\text{DNS}}}$  defined as

$$\lambda_{B_{\text{DNS}}} = \eta_{\text{DNS}} / \sqrt{Sc}. \quad (11)$$

where  $Sc(\mathbf{x}, t) = \nu(\mathbf{x}, t)/D$  is the dimensionless Schmidt number that varies in time and space, depending on the mixture. The Schmidt number  $Sc$  is greater than unity in the injection pipe and its vicinity, and in the zones of high helium concentration. However, the figure 4-b indicates that the Batchelor length scale  $\lambda_{B_{\text{DNS}}}$  is greater or of the same order than the employed mesh size  $\delta$  throughout the cavity.

The Kolmogorov length scale is thus the smallest one required in the present configuration. It is at most three times smaller than the mesh size  $\delta$ . To conclude, we consider that we perform a well-resolved simulation (that we will hereinafter call DNS), the mesh being fine enough to capture the main features of the flow and mixing dynamics.

#### 4.3. Identification of the buoyant-jet axis location

Identification of the buoyant jet axis is classically done through several quantities such as position of local velocity maxima, local scalar maxima, vorticity maxima, or by defining the jet axis as the time-averaged streamline [30]. It has been shown that the jet location is somewhat sensitive to these different criteria, in particular when moving away from the injection. In the present configuration, the strong confinement and the interaction with the enclosure walls (figure 2) make this determination even more difficult.

This is illustrated through the distribution of the time averaged vertical velocity component  $\langle u_3 \rangle_t$  at several heights (figure 5). It can be seen that the maximum  $\langle u_3 \rangle_t$  is clearly located on the axis in the potential cone of the jet up to  $z = 5$  cm (figure 5, (a) and (b)), despite the deviation of the jet by the cross-flow. Further downstream, black line contours highlight how the fluid - wall interaction gives rise to two symmetrical maxima before they re-connect after the jet separates from the wall (figure 5, (c) and (d)). Similar conclusions can be drawn from the  $\langle X_1 \rangle_t$  distribution (iso-contours shown later in section 6). Thus, an appropriate criterion should be employed to identify a continuous jet trajectory, particularly in the upper part of cavity.

As far as a turbulent plume is expected to develop in the upper part of the cavity and since buoyancy dominates in this zone, we pay attention to the quantity  $\langle \rho' u'_i \rangle_t g_i$ . This term appears in the conservation equation of the turbulent kinetic energy (TKE) if the Reynolds averaging approach is considered without introducing density weighted variables (Favre averaging) [31]. It denotes the buoyant production of TKE. In figure 6, the iso-contours of  $\text{rms}\{\rho\}_t$ ,  $\text{rms}\{u_3\}_t$  and  $\langle \rho' u'_3 \rangle_t g$  are presented respectively in the vertical mid-plane at  $y = 0$  for comparison.

The largest density fluctuations are mainly localized at the edges of the jet potential core and in the upper exterior region where the leaving mixture interacts with the heavy ambient fluid of the exterior environment. But smaller fluctuations (by about 60 % compared to their maximal value) are also present in the entire upper part of the cavity, both in the plume area and in the jet attachment zone. The velocity fluctuations are rather more clearly concentrated simultaneously within the cone jet, the plume in the upper part of the cavity and the attachment zone. However, it is noticeable that the buoyancy production

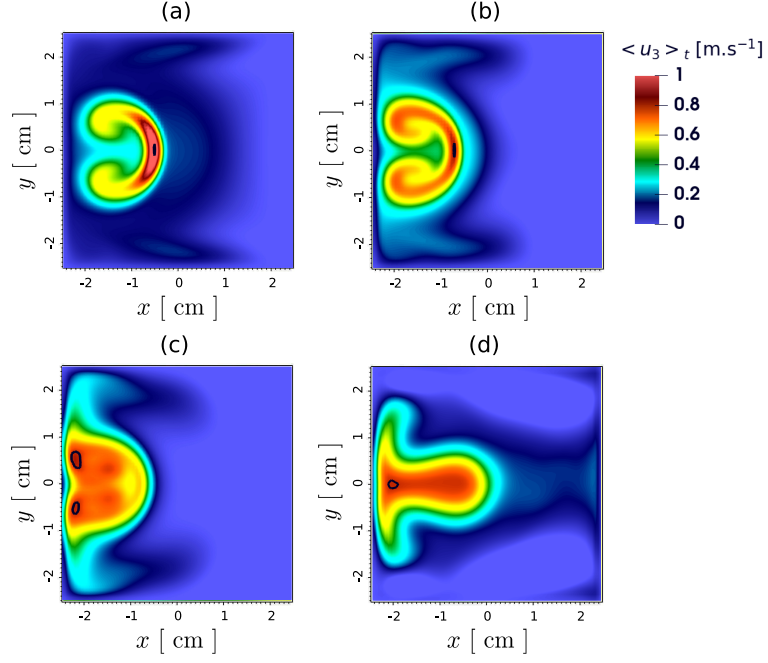


Figure 5: Time averaged vertical velocity component  $\langle u_3 \rangle_t$  iso-contours in four horizontal  $xy$ -plane sections. (a)  $z = 3$  cm, (b)  $z = 5$  cm, (c)  $z = 7$  cm, (d)  $z = 12$  cm. Black contours show the position of the maximum  $\langle u_3 \rangle_t$  value in the plane.

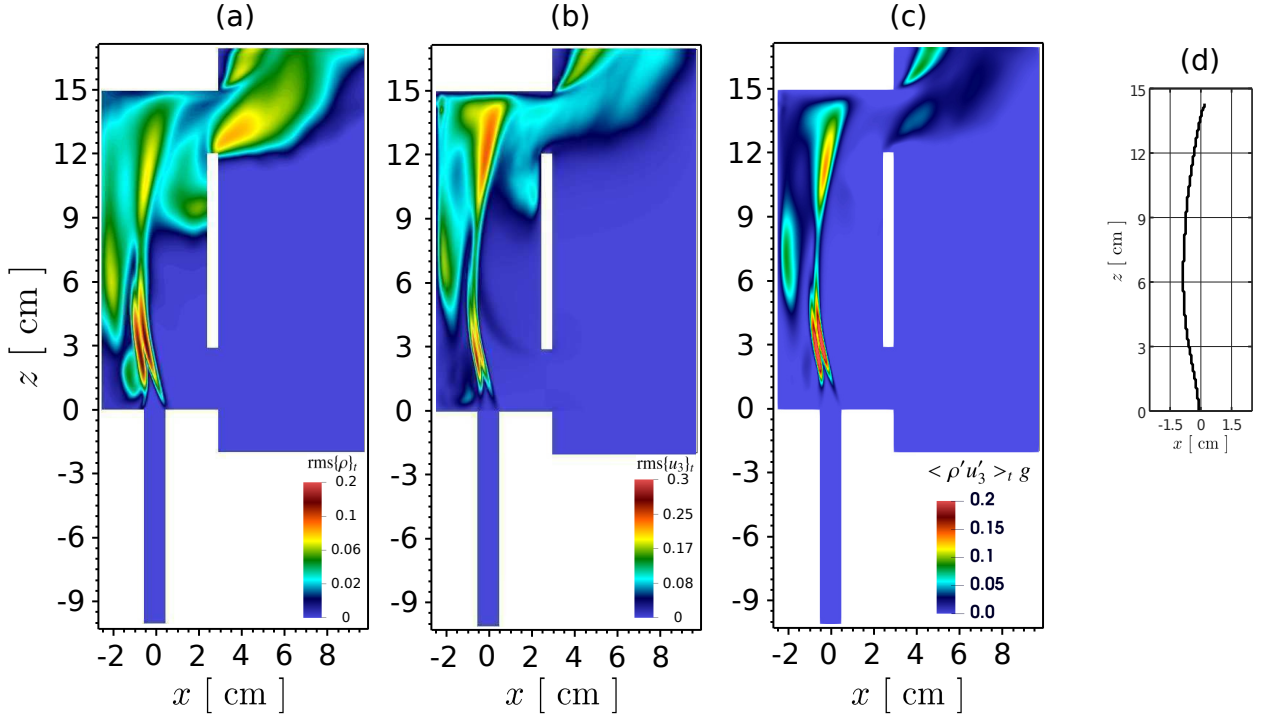


Figure 6: Iso-contours in the vertical mid-plane at  $y = 0$ . (a) mixture's density RMS ( $\text{rms}\{\rho\}_t$ ), (b) vertical velocity RMS ( $\text{rms}\{u_3\}_t$ ), (c) TKE buoyant production term ( $\langle \rho' u'_3 \rangle_t^R / g$ ), (d) time-averaged location of the jet axis.

term is much more sharply focused than the two previous quantities, on the buoyant jet development, from the edges of the cone jet to the plume establishment in the top part of the cavity. Nonetheless, the jet attachment zone also appears as a zone of TKE production, but to a lesser extent.

In view of these observations, we adopt the following strat-

egy to identify the buoyant jet trajectory. First, since the flow is symmetric with respect to the vertical mid-plane ( $y = 0$ ), we assume that the jet axis belongs to this plane. Second, since the jet potential core is well-defined by the time-averaged velocity, the axis location is defined as the position of the  $\langle u_3 \rangle_t$  local maximum up to  $z \leq 6$  cm, as commonly done for pure jet [30].

Finally, further downstream, we retain the local maxima of the turbulent mass flux  $\langle \rho' u_3' \rangle_t$  as the relevant quantity to mark the buoyant jet axis. We note the presence of an intermediate zone in between  $5.74 \leq z \leq 7.48$  cm, where both criteria give the same location. The resulting trajectory of the buoyant jet in the  $y = 0$  plane is displayed in figure 6-d, together with the corresponding numerical values in table 2.

#### 4.4. DNS-PIV comparisons

Let us first consider the normalized fluctuations of the vertical velocity component (see equation 8 for definition) in the lower part of the cavity. Figure 7 presents the  $u_3'^{,N}$  profile along the buoyant jet axis. Our previous LES results [20] are added to emphasize the improvement obtained by performing DNS. Indeed, contrary to LES, the turbulence level of the DNS results is of the same order than the PIV data, and even falls within the PIV error bars. The DNS fluctuations are at most 20% smaller in magnitude than the PIV ones. The spatial evolution of the DNS/PIV profiles are similar. These observations indicate that the DNS set-up is suitable for modeling the experiment in numerical terms but also in terms of physical modeling of the experimental injection conditions.

The profiles in figure 7 can also help to identify the approximate height ( $z_c$ ) at which the buoyant jet undertakes a laminar-to-turbulent transition. Following their DNS of a turbulent thermal plume, Plourde et al.[32] proposed that  $z_c$  coincides with the altitude of the first recorded maximum on the  $u_3'^{,N}$  profile. Clearly, the DNS/PIV both agree on a location of this transitional point around  $z_c = 3.5 - 4$  cm.

Figures 8 and 9 present a comparison of DNS and PIV results, based on several horizontal profiles of the magnitude of

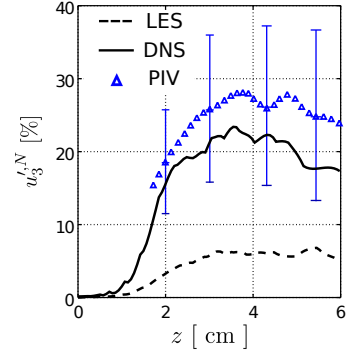


Figure 7: CFD-PIV normalized averaged vertical velocity fluctuations  $u_3'^{,N}$  along the inclined jet axis in the lower part of the cavity for  $0 \leq z \leq 6$  cm. Error bars represent the measurement-statistical accuracy of the PIV.

the time-averaged 2D velocity in two orthogonal planes, showing the buoyant jet development at different altitudes. Generally speaking, a good agreement of shape and magnitude is obtained up to the mid-height of the cavity ( $z \leq 7$  cm). The locations of the extrema are almost similar, despite the jet deviation initiated by the crossflow. This agreement is an interesting point because the 2D velocity magnitude contains a horizontal component of the velocity. Therefore, this reveals that the entrainment process is well approximated by the numerical modelling.

However, the velocity magnitude profiles are less consistent close to the ceiling ( $z = 14$  cm) with more dissimilar shapes. This zone corresponds to the buoyant jet reorientation into two large-scale rolls (as shown in section 6.1) and large fluctuations, which may be more difficult to capture experimentally or numerically due to the vicinity of both the ceiling and the upper

	Height $z$ [cm]	$x_{\text{axis}}$ [cm]	$\langle X_1 \rangle_t$ [%]	$\langle \rho \rangle_t$ [kg.m <sup>-3</sup> ]	$\langle u_3 \rangle_t$ [m.s <sup>-1</sup> ]	$\text{rms}\{\rho\}_t$	$\text{rms}\{u_3\}_t$
Bot vent	1	-0.179	99.82	0.163	1.98	0.0002	0.015
	2	-0.393	90.57	0.256	1.415	0.0379	0.223
	3	-0.604	72.7	0.436	0.964	0.079	0.259
	4	-0.744	56.57	0.599	0.819	0.074	0.199
	5	-0.813	43.41	0.731	0.746	0.049	0.142
	6	-0.883	34.31	0.823	0.631	0.028	0.107
	7	-0.813	30.86	0.858	0.66	0.023	0.068
	8	-0.813	31.89	0.847	0.67	0.029	0.043
	9	-0.744	33.65	0.829	0.745	0.045	0.084
	10	-0.604	32.98	0.836	0.769	0.058	0.144
	11	-0.464	32.37	0.843	0.777	0.062	0.184
Top vent	12	-0.321	31.32	0.853	0.759	0.059	0.209
	13	-0.179	30.15	0.865	0.732	0.053	0.213
	14	0.107	28.82	0.878	0.567	0.044	0.203

Table 2: DNS results along the inclined buoyant-jet axis located in the vertical mid-plane ( $y = 0.5$ ). Respectively the  $x$ - coordinate of the axis and the time averaged helium volume fraction  $\langle X_1 \rangle_t$ , density  $\langle \rho \rangle_t$  and vertical velocity component  $\langle u_3 \rangle_t$ ,  $\text{rms}\{\rho\}_t$  and  $\text{rms}\{u_3\}_t$ .

vent.

Finally, the vertical profiles of the time averaged velocity component normal to the vent surfaces ( $\langle u_1 \rangle_t$ ) are plotted in figure 10. For both vents, it is shown that the profile shape are in a good agreement. But the difference between the two profiles, that can be quantified in terms of 1D volume flow rate, shows an underestimation of the numerical estimation of the inflow or the outflow by approximately 15%. Note that it gives no indication about the overall volume flow rate, as the flow crossing the vents is not uniform in the  $y$ - direction and cannot be measured.

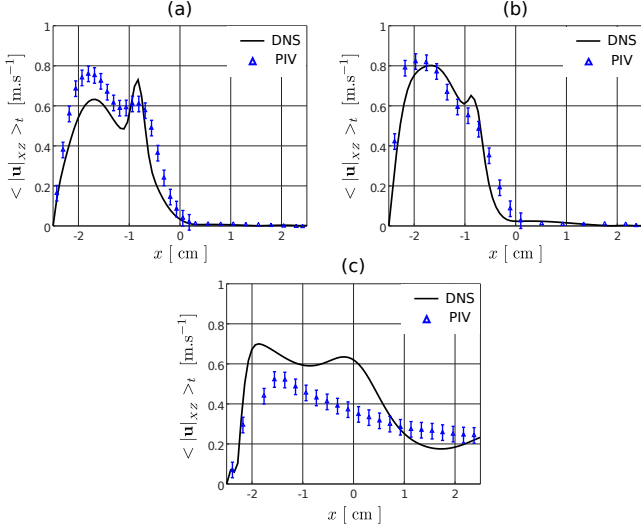


Figure 8: 2D time averaged velocity magnitude  $\langle |u|_{xz} \rangle_t$ , horizontal profiles along three  $x$ -lines at different altitudes: (a)  $(y = 0, z = 5.5\text{cm})$ , (b)  $(y = 0, z = 7\text{cm})$ , (c)  $(y = 0, z = 14\text{cm})$ . Error bars represent the measurement-statistical accuracy of the PIV.

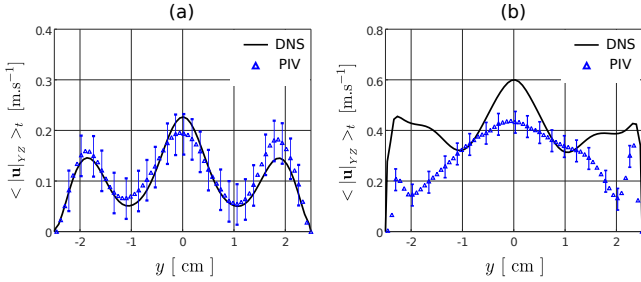


Figure 9: 2D time averaged velocity magnitude  $\langle |u|_{yz} \rangle_t$ , horizontal profiles along two  $y$ -lines at different altitudes: (a)  $(x = -0.5, z = 7\text{cm})$ , (b)  $(x = -0.5, z = 14\text{cm})$ . Error bars represent the measurement-statistical accuracy of the PIV.

## 5. DNS estimation of the plume fluxes and comparison with Morton et al.'s model

In this section, a macroscopic plume description based on the buoyant, mass and momentum fluxes is derived from the 3D DNS results. We aim to compare the DNS fluxes estimations with solutions obtained from the 1D model of Morton et al. [1] (MTT) to identify where and how far away the present flow

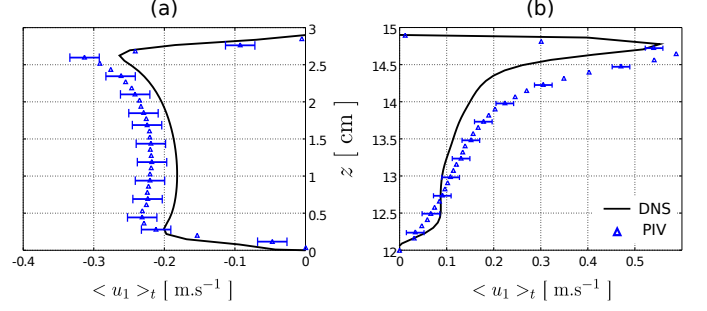


Figure 10: Vertical profiles of the time averaged horizontal velocity  $\langle u_1 \rangle_t$  along the line  $(x = 2.7, y = 0\text{ cm})$  crossing the (a) bottom vent, (b) top vent. Error bars represent the measurement-statistical accuracy of the PIV.

configuration is from the ideal case of a free thermal plume under the Boussinesq approximation.

### 5.1. The MTT model

The MTT theory models the plume spatial development in free environment with small density variations. It is based on the conservation equations of three global quantities: the fluxes of volume  $Q(z) = \int u_3 dS$ , momentum  $M(z) = \int u_3^2 dS$  and buoyancy  $B(z) = \int g u_3 (\rho_e(z) - \rho) / \rho_{\text{amb}} dS$ , where  $S$  is the horizontal cross-section of the plume, and  $\rho_e(z)$  is the vertical distribution of the environmental density far away from the buoyant jet.

Under the assumptions of a Gaussian distribution of the self-similar plume profiles, Boussinesq approximation and constant entrainment hypothesis  $\alpha$ , and integration in the horizontal cross-section, the conservation equations reduce to the 1D model :

$$\frac{dQ^{th}}{dz} = 2\alpha \sqrt{\pi M^{th}}, \quad (12)$$

$$\frac{dM^{th}}{dz} = \frac{B^{th} Q^{th}}{M^{th}}, \quad (13)$$

$$\frac{dB^{th}}{dz} = -N^2 Q^{th}, \quad (14)$$

where  $N$  is the Brunt-Väisälä stratification frequency defined as

$$N^2(z) = -\frac{g}{\rho_{\text{amb}}} \frac{d\rho_e}{dz}. \quad (15)$$

For a given value of  $\alpha$ , equations (eq. (12) - (14)) were integrated upwards starting from initial values at  $z = 0$  using a 4<sup>th</sup> order Runge-Kutta method.  $Q, M$  and  $B$  at  $z = 0$ , and the vertical distribution of the environmental density  $\rho_e(z)$  have been obtained from the DNS results. (see hereinafter for the estimation methodology).

## 5.2. Plume fluxes derived from DNS data

On the other hand,  $Q$ ,  $M$  and  $B$  may be obtained directly from the DNS data, using direct numerical integration :

$$Q^{num}(z) = \int_{\Omega_{DNS}} \langle u_3 \rangle_t dS, \quad (16)$$

$$M^{num}(z) = \int_{\Omega_{DNS}} \langle u_3 u_3 \rangle_t dS, \quad (17)$$

$$B^{num}(z) = \int_{\Omega_{DNS}} g \frac{\rho_e(z) \langle u_3 \rangle_t - \langle \rho u_3 \rangle_t}{\rho_{amb}} dS \quad (18)$$

where  $\Omega_{DNS}(z)$  is the  $z$ -dependent plume cross-section that is to be determined. Each horizontal plane is thus split into two parts: the inside of the buoyant jet  $\Omega_{DNS}$  and its complementary  $\bar{\Omega}_{DNS}$ , namely the far-field or environment outside the jet. Inside  $\bar{\Omega}_{DNS}$ , the mixture density  $\rho_e(z)$  is taken homogeneous and is computed as the 2D space and time average on this specific area.

As the plume axis is not straight, a specific methodology has to be applied to define  $\Omega_{DNS}$ . We consider a Gaussian distribution of  $\langle u_3 \rangle_t$ ,

$$u_3(r, z) = u_{3G}(z) \exp(-r^2/b_G^2(z)). \quad (19)$$

where  $u_{3G}(z)$  and  $b_G(z)$  correspond to the characteristic values of the vertical velocity and the radius of the jet respectively. The area based on  $b_G(z)$  is called  $\sigma$ . As the three fluxes  $Q$ ,  $M$  and  $B$  depend explicitly on  $u_3$ , the criterion to define the integral zone  $\Omega_{DNS}(z)$  is linked to the time-averaged vertical velocity field  $\langle u_3 \rangle_t$ . Taking the maximum value of  $\langle u_3 \rangle_t$  over the horizontal plane ( $z$ ) as an estimate of  $u_{3G}(z)$ , we set

$$\Omega_{DNS}(z) = \{(x, y) \mid \langle u_3 \rangle_t(\mathbf{x}) \geq \varepsilon_{u_3} \cdot u_{3G}(z)\}, \quad (20)$$

with  $\varepsilon_{u_3}$  is a threshold value. Since the so-determined integration zone  $\Omega_{DNS}(z)$  does not cover the entire plume area, correction factors are applied to recover the nominal quantities from these numerical values :

$$Q^{DNS} = \frac{1}{1 - \varepsilon_{u_3}} Q^{num}, \quad (21)$$

$$M^{DNS} = \frac{1}{1 - \varepsilon_{u_3}^2} M^{num}, \quad (22)$$

$$B^{DNS} = \frac{g}{\rho_{amb}} (\rho_e Q^{DNS} - Q_m^{DNS}), \quad (23)$$

where  $Q_m^{DNS}$  is the mass momentum flux calculated from DNS by the following relation

$$Q_m^{DNS}(z) = Q_m^{num}(z) \frac{\rho_e(z) + \rho_G(z)}{(1 - \varepsilon_{u_3})^2 \rho_e(z) + (1 - \varepsilon_{u_3}^2) \rho_G(z)} \quad (24)$$

where  $Q_m^{num}(z) = \int_{\Omega_{DNS}} \langle \rho u_3 \rangle_t dS$  and  $\rho_G(z)$  is the characteristic density value from the Gaussian profile of  $(\rho_e - \rho)$  inside the buoyant jet.

Figure 11 illustrates the influence of  $\varepsilon_{u_3}$  on the approximation of the integration zone  $\Omega_{DNS}$  with three threshold values,  $1/e$ ,  $1/e^2$  and  $1/e^3$  where  $e$  is the Euler's number, corresponding

to one, two and three times  $\sigma$  (noted  $1\sigma$ ,  $2\sigma$ ,  $3\sigma$ ) respectively. While at the two lowest planes ( $z = 3$  and  $8$  cm), the choice of  $\sigma$  appears a reasonable approximate of the plume region for  $\langle \rho \rangle_t$ , it is not so clear for the vertical velocity  $\langle u_3 \rangle_t$ , where a part of the rising flow is missed by  $\sigma$ . Additionally, the top part of cavity (see for instance  $z = 12$  cm) is more complicated, particularly regarding the estimate of the presumed uniform environment density  $\rho_e(z)$  based on  $\bar{\Omega}_{DNS}$ . Indeed, this zone is more homogeneous in species than at lower altitudes. We finally retain the integration zone  $3\sigma$ , which covers an area larger than the plume region but provides a better estimate of  $\rho_e(z)$ .

## 5.3. Comparison between the DNS and theoretical profiles

Integration of the 1D theoretical model (eq. (12) - (14)) requires that the entrainment coefficient  $\alpha$  be fixed. As recalled earlier,  $\alpha$  ranges from 0.07 to 0.09 for jets, and 0.12 to 0.17 for plumes (see for a review [33]). Since the physical configuration considered here does not belong to either category, no *a priori* value can be prescribed for  $\alpha$ . Therefore, we use the two approaches independently (DNS and theoretical modelling) to estimate  $\alpha$  by minimizing by trial and error the difference between both approximations  $B^{DNS}$  and  $B^{th}$  over the entire height of the cavity. We choose the buoyant flux since it is the only quantity which is directly related to the ambient environment outside the buoyant jet through the density  $\rho_e$ . The best agreement between the two  $B$ -profiles was obtained for  $\alpha = 0.07$ . This is quite surprising as this value corresponds to a pure jet [7, 33], which as already said does not quite correspond to our configuration.

On figures 12-a,b), we note that the buoyant flux  $B$  and the ambient density  $\rho_e$  profiles follow very similar trends and both present a quasi-linear vertical distribution near the middle of the cavity. From this, three layers can be distinguished in terms of air-helium mixture in the outer environment of the jet ( $\rho_e$ ) and as a result of buoyancy flows ( $B$ ). First, for  $z \lesssim 8$  cm (labelled *H1*), the buoyancy flux is nearly constant and corresponds to a quasi-homogeneous zone in which the environmental density  $\rho_e$  is close to that of pure air  $\rho_{amb}$  with a variation of less than 5%. A second quasi-homogeneous zone is found at the top of the cavity (for  $z \gtrsim 12$  cm, labelled *H2*), where  $B^{DNS}$  is almost equal to zero. In between, one observes a linearly stratified layer ( $8 \lesssim z \lesssim 12$  cm, labelled *S*) where  $B$  and  $\rho_e$  vary quasi-linearly.

Unlike  $B$ , the profiles of  $M$  and  $Q$  from both calculations (figures 12-c,d) are very dissimilar, especially for  $Q$ . The theoretical model gives positive monotonic evolutions of  $Q$  and  $M$  with ( $z$ ), while the DNS estimation provides more informative insights into the vertical development of the flow structure. Four zones (or development stages) can be distinguished from  $Q^{DNS}$ . First, we recognize the injection zone until  $z \approx 2$  cm, where the buoyant jet behaves like a jet (figure 2). In this zone,  $Q$  is well estimated by the MTT model. This first stage is called the *J* zone. It is followed by a sudden increase of  $Q^{DNS}$  up to  $z \approx 3$  cm, showing the effect of the cross-flow in entrainment processes that the MTT model cannot predict. This zone ( $2 \lesssim z \lesssim 3$ ) cm is called *CF*.

Similarly, a good agreement between  $Q^{th}$  and  $Q^{DNS}$  is obtained in a thin layer ( $10 \lesssim z \lesssim 12$  cm, called *P* stage) inside the stratified zone. From figure 6, we can associate the *P* stage with the establishment of a turbulent plume. Additionally, the location of the buoyant-jet axis is situated at the same horizontal position ( $x_{axis}$ ) at altitudes  $z = 3$  and  $z = 10$  cm (see table 2), which explains how the MTT model can recover a good approximate of  $Q^{DNS}$  from  $z = 10$  cm. Above the *P* stage, we notice a rapid increase followed by an abrupt decrease of the  $Q$  and  $M$  fluxes revealing the presence of an exiting flow from the cavity ( $z \gtrsim 12$  cm, called *E* zone). Finally, inside a large middle part of the cavity, an unusual zone appears ( $3 \lesssim z \lesssim 10$  cm, called *B* zone). It corresponds to a large plateau, where  $Q$  is kept constant and  $M$  increases monotonically. This can be interpreted as a blocking zone, where no entrainment is possible and the unique way for  $M$  to increase is through the increase turbulent fluctuations (figure 6).

To conclude, it is clear that the buoyant jet development does not follow the MTT model, despite the good agreement between  $B^{th}$  and  $B^{DNS}$  and the presence of the quasi-homogeneous layer *H1* at the bottom part of the cavity. This mismatch is mainly due to the strong confinement of the buoyant jet leading to the appearance of both cross-flow *CF* and blocking *B* stages, as shown in the  $Q$  profiles. But the disagreement between the  $M^{DNS}$  and  $M^{th}$  profiles was foreseeable because of the difference in densities of helium and air: it indeed makes the Boussinesq approximation (used in the equation 13) invalid.

## 6. Flow analysis and discussion

The global fluxes calculation from DNS and the above comparison with theory have been instructive to broadly define the different stages of flow structure. Now, we analyse the flow with a more local point of view in order to depict how the combination of the jet confinement and the natural ventilation modifies the flow pattern and the helium distribution. Finally, a discussion about the basic assumptions of the classic ventilation model of Linden [12] is proposed to reveal the specific features of the present study case.

### 6.1. Vertical evolution along the jet axis

The development of the buoyant jet along its axis is illustrated by considering both the mean and rms values of the helium mass fraction, the mixture density and the vertical velocity on figures 13 and 14. Values at evenly distributed altitudes are also given in table 2 for the sake of completeness. Additional information that could potentially be used to validate numerical codes is placed in the Appendix. In what follows, the location of the different flow zones identified in the previous section are marked on the figures.

First, we consider the time-averaged profiles (figure 13). As expected in a light jet, we observe the monotonic decrease of the time-averaged helium mass fraction ( $X_1$ ) and the vertical velocity ( $u_3$ ) with increasing altitude ( $z$ ) up to about the top of the lower homogeneous layer ( $z_{H1}$ ). Above this altitude, a weak increase of  $u_3$  marks the transition jet - plume until a kind of plateau in the plume zone (P). In the exit zone (E) of the

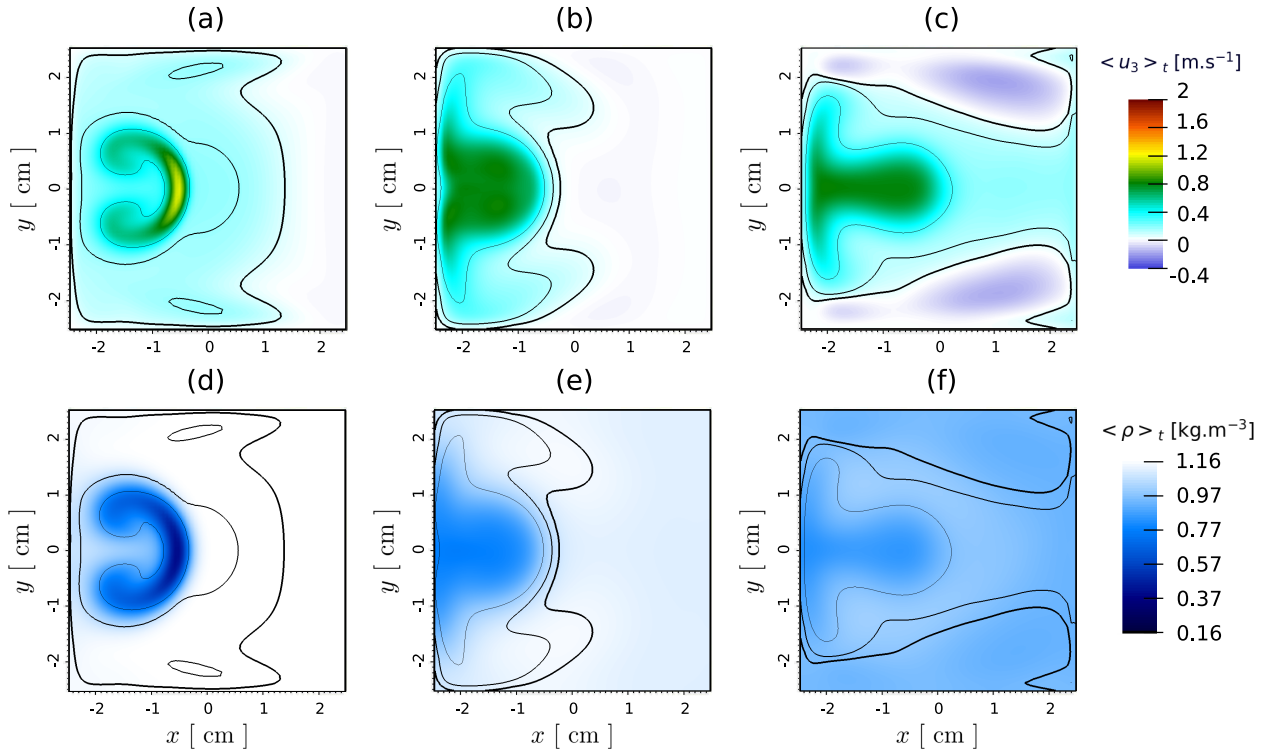


Figure 11:  $\Omega_{DNS}(z)$  integrating zone with  $\varepsilon_{u_3} = 1/e, 1/e^2$  and  $1/e^3$  corresponding to  $\sigma, 2\sigma$  and  $3\sigma$  respectively, at three horizontal planes. (a,b,c) Time-averaged vertical velocity  $\langle u_3 \rangle_t$  iso-contours. (d,e,f) Time-averaged mixture density  $\langle \rho \rangle_t$  iso-contours. (a,d)  $z = 3$  cm, (b,e)  $z = 8$  cm, (c,f)  $z = 12$  cm. The thickness of the iso-contour lines increases with  $\varepsilon_{u_3}$ .

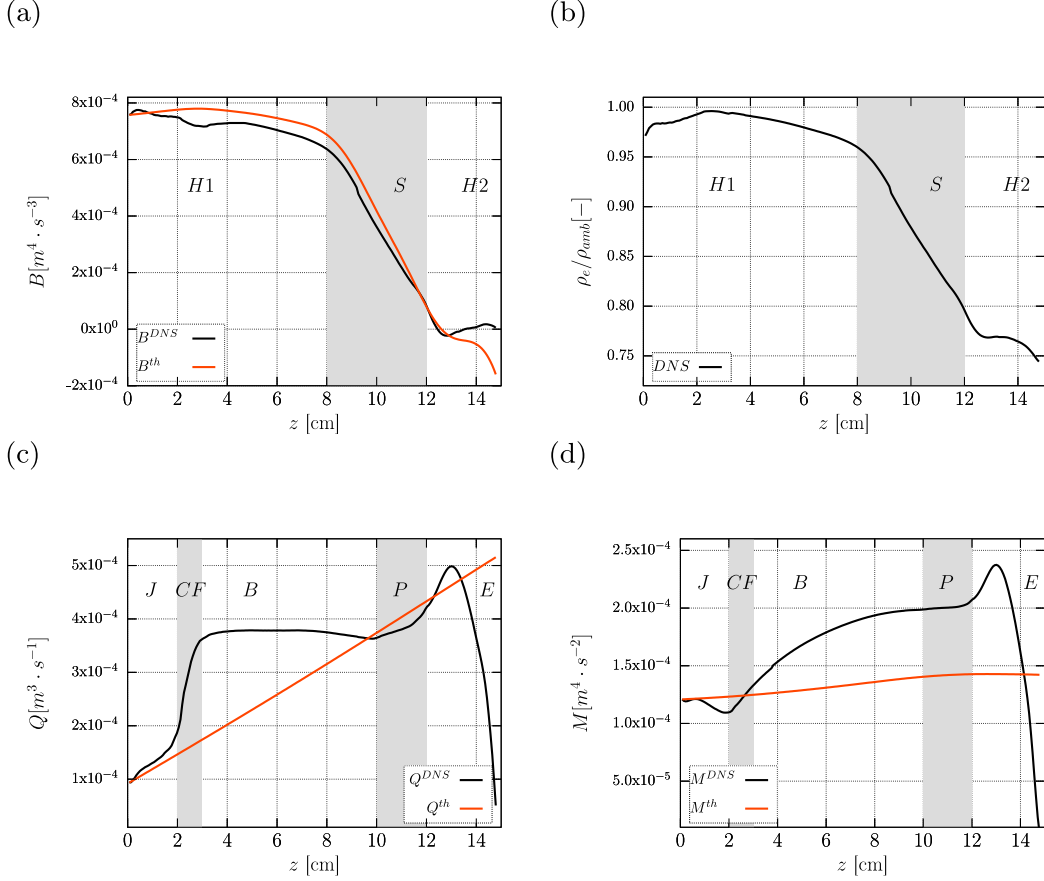


Figure 12: Vertical distributions of the global fluxes: (a) buoyancy flux  $B$  (top left); (b) dimensionless environmental density  $\rho_e/\rho_{amb}$  (top right); (c) volume flux  $Q$  (bottom left); (d) momentum flux  $M$  (bottom right). DNS integral values are in black, solution of 1D MTT model (equations (12) to (14)) are in red. The dashed areas indicate the flow layers as defined in section 5.3.

mixture,  $u_3$  abruptly decreases close to the ceiling due to the presence of large counter-rotating vortices, as shown on figure 15. These large-scale rolls are almost the same size as the height of the top vent, and completely fill the top of the cavity. Note that the vertical profile of the mixture density ( $\rho$ ) is directly related to the  $X_1$  through the use of the state law (equation 4). However, we plot its shape to complement the next figure.

The definition of the vertically stacked zones of the flow structure, previously proposed in section 5.3, is more meaningful when considering the vertical distribution of fluctuations along the jet axis (figure 14). Here, we retain the normalized fluctuations  $\rho'^N$  as a representative quantity of the mixture properties. The influence of the cross-flow is clearly seen on the fluctuations of density, velocity or the production term of turbulent kinetic energy by buoyancy ( $G_b = g\langle\rho u'_3\rangle_t$ ) in the zone CF where two effects add up (increase of the shear and the helium-air mixing) due to the confluence of fresh air horizontal inflow from the bottom vent with the upward helium jet. Moreover, we note that the peak of fluctuations of  $u'_3$  is reached close to  $z = 4$  cm and particularly marked for  $G_b$ , illustrating the turbulent transition of the jet, as already mentioned in section 4.4. Above CF, all the fluctuations decrease until the jet-plume transition at around  $z_{H1}$ . At this altitude, the weak increase of both  $X_1$  and  $u_3$  is accompanied by a sudden increase

of all fluctuating quantities. However, while  $u'_3$  continues to increase up to near the ceiling, mixture density fluctuations are largest in the P zone, and  $G_b$  peak is located at the bottom of the second homogeneous layer  $z_{H2}$ . To conclude, the stratified zone (between  $z_{H1}$  and  $z_{H2}$ ) appears to be a fluid zone of intense turbulence production where the turbulent plume develops.

## 6.2. Helium distribution

In the previous section, the vertical evolution of the buoyant jet has been described locally along the jet axis. However, the vertical development of the buoyant jet depends largely on the environment density  $\rho_e$ . In this section, we aim to give an insight into the helium distribution within the cavity, which is more inhomogeneous than suggested by  $\rho_e(z)$  in section 5.2.

First, the distribution of the time averaged helium mass fraction  $\langle X_1 \rangle_t$  on four vertical 2D planes is displayed on the figure 16. Note again the symmetry of the time-averaged distributions in the plane  $(y, z)$ . Despite the asymmetry due to the vertical vents, the jet (J), cross-flow (CF), fluid exit (E), and even the plume (P) zone can be considered as acceptable definitions of the classic development stages of a buoyant jet within a vented cavity. However, the intermediate blocking (B) zone ( $3 \lesssim z \lesssim 10$  cm) is more remarkable. This fluid volume is clearly divided in two horizontally stacked parts. The first one,

close to the vents, is mainly filled by fresh air, while the second part undergoes an accumulation of helium. This phenomenon can be explained by the jet attachment to the vertical wall opposite to the vents by Coanda effect (from  $z \geq 4$  cm), which originates from the jet deviation due to the cross-flow from the bottom vent. The jet deformation by the cross-flow and the jet attachment to the vertical wall are obvious on the figure 17 as illustrated by the  $\langle X_1 \rangle_t$  iso-contours on the four horizontal planes previously considered in figure 5. We recognize the classic pattern of jet in a cross-flow up to  $z = 5$  cm in agreement with the  $\langle u_3 \rangle_t$  distribution. As a result of the jet attachment on the left wall, an helium accumulation is present at  $z = 7$  cm, which tends to persist until the turbulent plume (P zone) appears (not shown here), promoting mixing processes. Consequently, within the P and E zones ( $z > 10$  cm), the  $\langle u_3 \rangle_t$  and  $\langle X_1 \rangle_t$  distributions lost their coherence. While the time-averaged velocity field keeps its main well-organized structure, the scalar field becomes more homogeneous.

More quantitative conclusions can be drawn from the profiles of  $X_1$  along nine vertical lines throughout the cavity of figure 18. Eight of these lines are straight and referred to by the profiles along points (1) to (8) (see the crosses and the labels on figure 17-d that depict their positions in the horizontal plane). The profile along point (9) corresponds to that along the inclined buoyant-jet axis. It is clear that above  $z = H_2$ , the helium mass fraction is very homogeneous as expected, with  $X_1 \sim 30\%$ . Similarly, except along the jet axis, the fluid volume

is mainly filled by fresh air below  $z = H_1$ . But in the blocking zone (B), we observe the  $X_1$  increase at a particular location (point 8), which is located between the wall and the jet axis. At this point, the increase is even critical from a safety point of view, as  $X_1$  along the line (8) is higher (until +40%) than its value along the jet axis. It means that, even when there is no obstacle inside the cavity, the flow structure can create conditions of helium accumulation. The appearance of the turbulent plume (P) here is what stops the phenomenon.

In the upper part of the blocking zone, the stratified layer (S) settles, which is supposed to result from the large inflow flow rate entering inside the cavity through the bottom vent, as proposed by [14]. But this layer is not taken into account in the classic two-layer stratification models of ventilation, such as the Linden et al. model [11]. The issue of the non-compliance of the present configuration with the well-known basic assumptions of classic theoretical models is the purpose of the following section.

### 6.3. Discussion: comparison between DNS results and the Linden et al.'s ventilation model

The ventilation model of Linden et al. [11] can be used to predict the mixture density in the top part of a emptying-filling box. This model assumes a two-layer concentration stratification in the cavity where the interface height separating the two layers has to be determined. The upper part of the cavity is filled with an homogeneous layer of two fluid mixture while the bot-

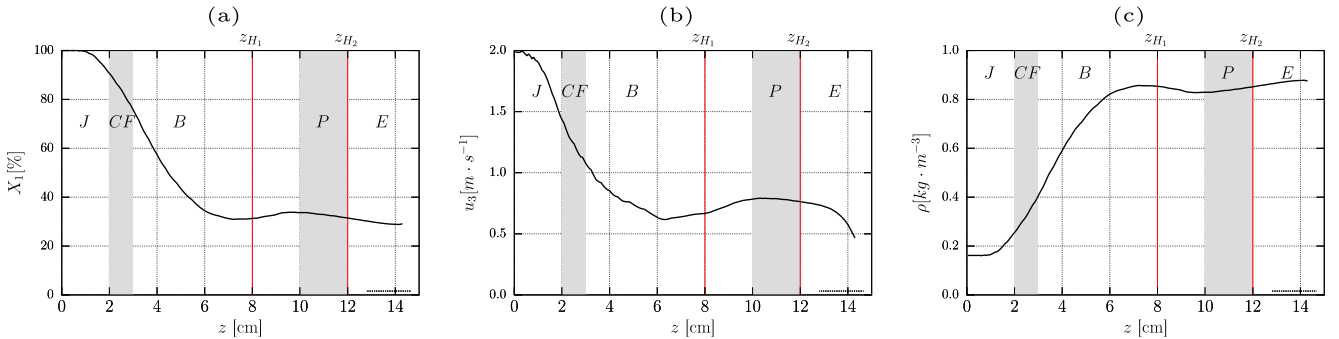


Figure 13: Time averaged profiles along the buoyant jet axis. (a) helium volume fraction  $\langle X_1 \rangle_t$ , (b) vertical velocity  $\langle u_3 \rangle_t$ , (c) density  $\langle \rho \rangle_t$ . The dashed areas indicate the flow layers as defined in section 5.3. The edges of the two quasi-homogeneous layers  $H_1$  and  $H_2$  are marked by red lines.

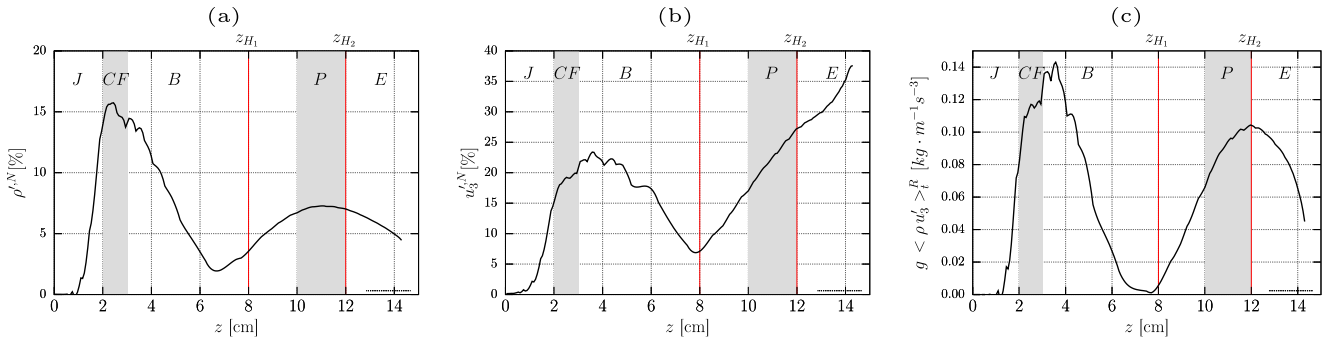


Figure 14: Fluctuating vertical profiles along the buoyant jet axis. (a) density normalized fluctuations  $\rho'^N$ , (b) vertical velocity normalized fluctuations  $u_3'^N$ , (c) Buoyancy turbulent production  $G_b = g \langle \rho u_3' \rangle_t$ . The dashed areas indicate the flow layers as defined in section 5.3. The edges of the two quasi-homogeneous layers  $H_1$  and  $H_2$  are marked by red lines.

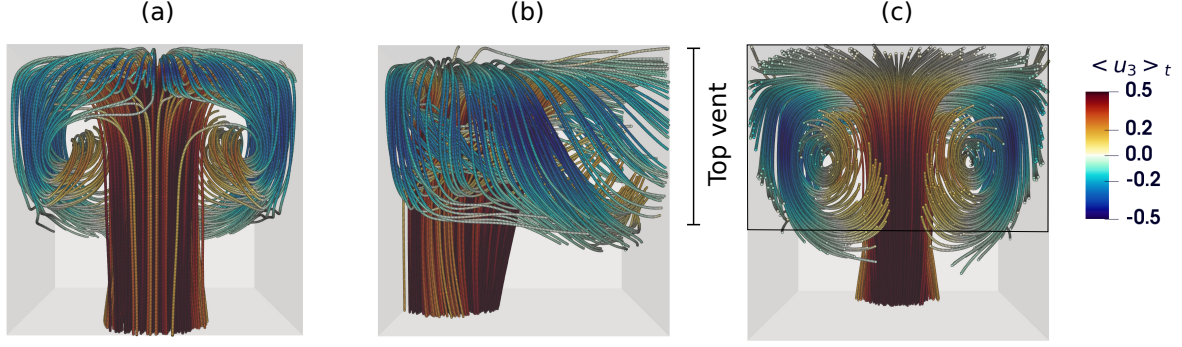


Figure 15: Time averaged velocity magnitude streamlines in a zoomed region at the top of the cavity. (a) back view, (b) side view, (c) front view.

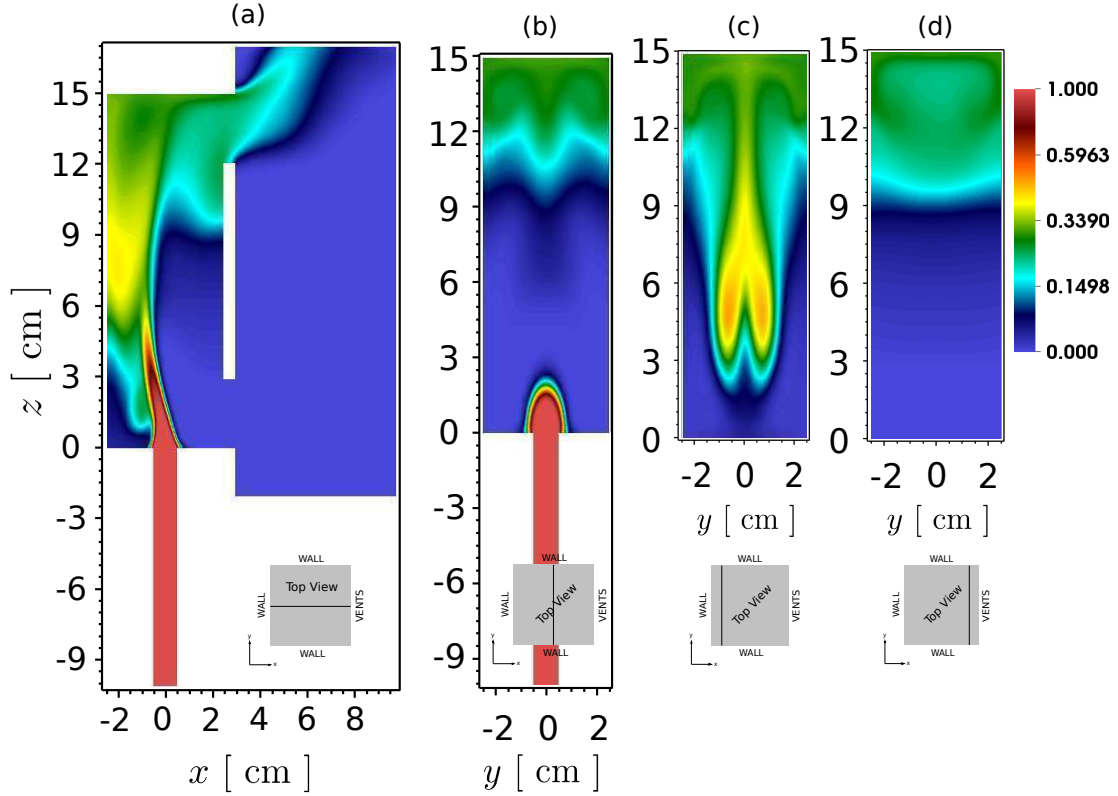


Figure 16: Time averaged helium volume fraction  $\langle X_1 \rangle$  iso-contours in vertical 2D sections. (a) mid-vertical  $xz$ -plane ( $y = 0$ ), (b) mid-vertical  $yz$ -plane ( $x = 0$ ), (c) vertical  $yz$ -plane ( $x = -2$  cm), (d) vertical  $yz$ -plane ( $x = 2$  cm).

tom part corresponds to a fresh air environment with density  $\rho_e = \rho_{\text{amb}}$ .

Let us first recall that this model is based on the analytical solutions of the MTT system (eq. 12 to 14), and thus on the Boussinesq approximation. The resulting volume flux depends on altitude  $z$  as

$$Q(z) = C(\alpha)B_0^{1/3}z^{5/3}. \quad (25)$$

where  $C(\alpha) = \frac{6}{5} \left(\frac{g}{10}\right)^{1/3} \pi^{2/3} \alpha^{4/3}$  is a constant related to the entrainment coefficient  $\alpha$ ,  $B_0$  the buoyancy flux at the injection ( $B_0 = Q_{v,0} g(\rho_{\text{amb}} - \rho_{\text{inj}})/\rho_{\text{amb}}$ ) and  $Q_{v,0}$  the injection volume flux.

This relationship is used to determine the interface height  $z_i$  and the mean density  $\rho_i$  in the upper homogeneous layer. By applying the global conservation of the volume flux in the cav-

ity, the implicit relationship for  $z_i$  is finally obtained

$$\frac{z_i^5}{H - z_i} = \frac{A^{*2}}{C^3(\alpha)} \quad (26)$$

with  $A^* = \sqrt{c_{\text{out}} S_{\text{in}} S_{\text{out}}} \sqrt{\frac{1}{2} \left( \frac{c_{\text{out}}}{c_{\text{in}}} S_{\text{out}}^2 + S_{\text{in}}^2 \right)}$  the effective opening surface, related to the areas of two openings  $S_{\text{in}}$ ,  $S_{\text{out}}$  and their pressure-loss coefficients  $c_{\text{in}}$ ,  $c_{\text{out}}$ . Here, we assume small openings, i.e.  $c_{\text{in}} = c_{\text{out}} = 0.5$ . The entrainment coefficient is taken equal to  $\alpha = 0.07$  following the estimation from our DNS results (section 5.3). The mixture density  $\rho_i$  can then be estimated by

$$\rho_i = \rho_{\text{amb}} \left( 1 - \frac{1}{gC(\alpha)} B_0^{2/3} z_i^{-5/3} \right). \quad (27)$$

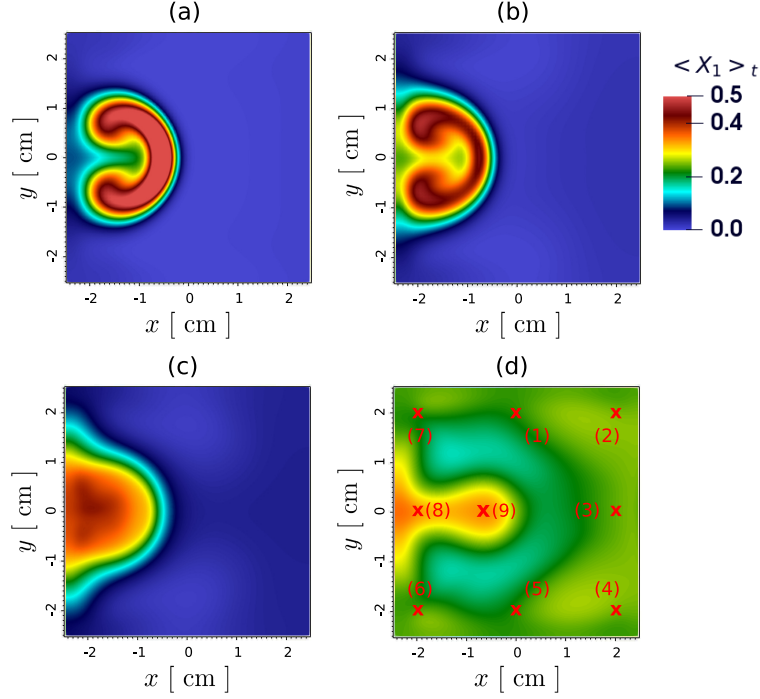


Figure 17: 2D time averaged helium volume fraction  $\langle X_1 \rangle_t$  iso-contours in four horizontal  $xy$ -planes. (a)  $z = 3$  cm, (b)  $z = 5$  cm, (c)  $z = 7$  cm, (d)  $z = 12$  cm. Crosses and numerals present on the subfigure (d) designate the location of the vertical lines used in figure 18.

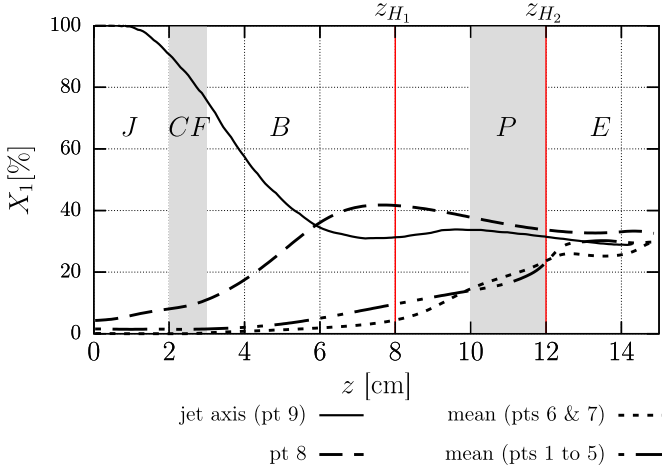


Figure 18: Vertical distributions of the time-averaged helium mass fraction  $\langle X_1 \rangle$  along either the jet axis or a particular vertical line (point 8). The  $\langle X_1 \rangle$  mean distributions between two symmetrical lines are also plotted for two particular locations of the cavity. Labels 1 to 9 correspond to the vertical lines, as shown in figure 17. The shaded areas indicate the flow layers as defined in section 5.3. The edges of the two quasi-homogeneous layers  $H1$  and  $H2$  are marked by red lines.

The values of interface height  $z_i$  and homogeneous density  $\rho_i$  obtained from DNS results and from the theoretical model (eq. 26 and 27) are reported in Table 3. For the DNS values,  $z_i$  was taken as  $z_{H2}$ , and  $\rho_i$  is the spatial average of  $\rho$  for  $z \geq z_i$ . The helium volume fraction  $X_1^i$  within the homogeneous layer is then obtained from equation (7).

Although we have used Linden et al.'s model far out of its domain of validity, its predictions of the altitude and density of

Parameters	DNS	Linden's model	Relative error [%]
$z_i$ [cm]	12	13.4	+12%
$\rho_i$ [kg.m <sup>-3</sup> ]	0.87	0.77	-11%
$X_1^i$ [%]	29.6	39.5	+33%

Table 3: Characteristic values of the upper homogeneous layer. Comparison between DNS results and the theoretical predictions using the Linden et al. [11] model.

the upper homogeneous layer are only 10% away from DNS results, the model predicting a thinner upper layer filled with a lighter mixture. However, this corresponds to a large overestimate of the helium volume fraction. This fairly good concordance is somewhat unexpected since our configuration displays some specific features which obviously do not correspond to the assumptions of the theoretical model, namely: i) no bi-layer concentration distribution due to important confinement effect ; ii) the Boussinesq approximation does not hold due to a large density ratio ( $\rho_{air}/\rho_{He} \approx 7.3$ ); iii) the small injection assumption is not verified as the outlet flux through the top vent (19.62NL/min) is only four times larger than the injection flux (5NL/min). Nonetheless, an attempt to explain this roughly good agreement can be given based on figure 12. Indeed, at interface level  $z_i$ ,  $Q^{th}$  and  $Q^{DNS}$  are quite close, while  $Q^{th}(z_i)$  is used in the global balance of volume fluxes over the whole cavity to approach  $z_i$ . This illustrates the key role of the upward volume flow rate across the H2 interface in the mixture composition of the homogeneous layer, as proposed by Linden et al.

## 7. Concluding remarks

We have performed direct numerical simulations (DNS) of a light buoyant helium jet developing in a two vented cavity. The grid size was taken small enough to capture reasonably well both the Kolmogorov dissipation and species mixing Batchelor length scales. Along the lines of a previous study, the computational domain was designed to encompass a sufficiently large exterior region allowing to set the numerical boundary conditions far enough so that the natural inlet/outlet conditions are satisfactorily approached. The quality of the DNS simulations is further assessed by comparisons of the DNS data with particle image velocimetry measurements which show a satisfactory agreement both for the time-averaged and fluctuating fields.

A thorough description of the complex time-averaged flow pattern is presented. The buoyant jet from the floor is bent by the strong crossflow from the lower vent until it touches the back wall of the cavity. Its cross section shows the corresponding crescent shape resulting from embedded counter rotating vortices. The jet remains attached to the back wall up to past mid-height. Further up, the flow separates from the wall and gives rise to a 3D donuts shape recirculating zone that swirls out from the upper vent. A mixed criterion based on the maximum vertical velocity and the turbulent buoyancy production is proposed to track the spatial position of the deviated jet axis all along the cavity height.

The DNS data were used to compute the usual macroscopic quantities  $B$ ,  $Q$ ,  $M$  that classically characterize the buoyant jets. Several tests were made to determine a criterion resulting in the most appropriate cross section integration zone, also allowing for the determination of the exterior region and thus to the ambient density. This allowed to integrate numerically the 1D MTT model and the best value of the entrainment coefficient was obtained through minimization of the difference on the buoyancy flux. Comparison of the DNS fluxes with solutions obtained from the 1D MTT model made possible to identify i) a three layer horizontal structure of the helium distribution within the cavity, with a linearly stratified layer in between two homogeneous layers ; ii) five horizontal stages describing the buoyant jet development from the zones of jet - cross flow interaction to the plume stage and finally the exit zone, including at intermediate altitudes, a blocking zone where the momentum flux remains quasi-constant.

This five stage description of the buoyant plume development is confirmed by the vertical evolution of the time-averaged and fluctuating quantities along the jet axis. However the helium distribution within the cavity is much less homogeneous than suggested by the global flux approach. Specifically, helium accumulates in the blocking zone with a concentration about a third larger than on the jet axis or in the upper homogeneous layer. This indicates that even if no physical obstacle is present in an emptying-filling box, the flow pattern can result in helium accumulation conditions. Finally, we apply Linden et al.'s model far out of its domain of validity. Yet its predictions of the altitude and density of the upper homogeneous layer are only 10% away from DNS results. However, this results on a larger error on the estimate of the helium volume fraction. This

work shows the difficulty to predict with accuracy the helium spatial distribution in a highly-confined two-vented enclosure, especially for large density ratio. In particular helium concentration measurements are needed to confirm the possible existence of local maxima of concentration around mid-height.

## Acknowledgements

This work was granted access to the HPC resources of IDRIS under allocations 2a-0326 attributed by GENCI (Grand Equipement National de Calcul Intensif). This work has benefited from the financial support of the LabeX LaSIPS (ANR-10-LABX-0032-LaSIPS) managed by the French National Research Agency under the "Investissements d'avenir" program.

## Appendix: DNS reference values and profiles

### Helium concentration

We start first by considering the time averaged helium volume fraction field  $\langle X_1 \rangle_t$ . Quantitative horizontal and span-wise profiles are considered in figure 19 for  $y = 0$  (top-bottom pair, left) and  $x = -0.5$  cm (top-bottom pair, right). The lower horizontal profiles can be served to define the position of the inclined buoyant-jet axis (can be assumed at the maximum concentration). The almost-symmetrical distribution in the span-wise profiles is seen again at all heights as far as the deviation only takes place towards the left wall facing the vents.

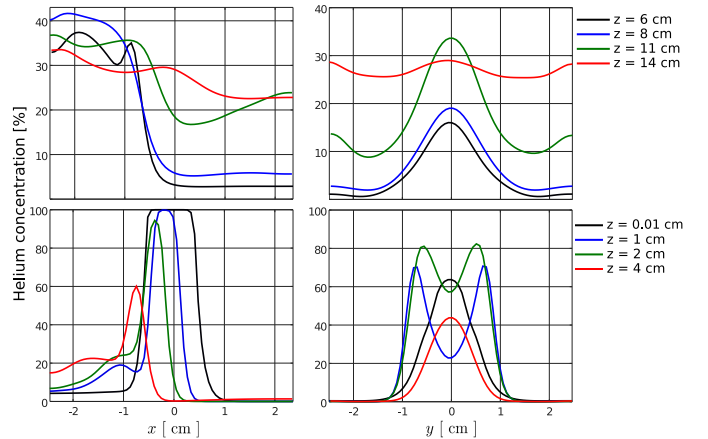


Figure 19: Horizontal and span-wise time averaged helium volume fraction  $\langle X_1 \rangle_t$  profiles at heights  $z = 0.01, 1, 2, 4$  cm (bottom series) and  $z = 6, 8, 11, 14$  cm (top series). Left top-bottom pair:  $y = 0$  cm, right top-bottom pair:  $x = -0.5$  cm.

In table 4, the maximum values of  $\langle X_1 \rangle_t$  in several horizontal  $xy$ -planes situated at 15 different heights are presented with their corresponding  $(x, y)$  coordinates. We can clearly note that the maximal values are positioned in the vicinity of the mid-vertical  $xz$ -plane ( $y = 0$ ) that contains the inclined buoyant-jet axis. Above  $z = 12$  cm, the maximum is around 33 % as reported previously in the top-formed homogeneous layer.

Height $z$ [cm]	Helium volume fraction $\langle X_1 \rangle_t(x, y, z)$	
	Maximum value in the $xy$ -plane [%]	Location $(x, y)$ [cm]
1	99.84	(-0.119, -0.024)
2	94.384	(-0.333, 0.048)
3	78.36	(-0.546, 0.048)
4	60.087	(-0.686, 0.048)
5	47.385	(-1.939, 0.753)
6	43.828	(-2.079, 0.546)
7	41.398	(-1.939, 0.048)
8	41.653	(-2.079, 0.048)
9	40.377	(-2.218, 0.048)
10	38.635	(-2.288, 0.048)
11	36.808	(-2.357, 0.048)
12	35.091	(-2.357, 0.048)
13	33.991	(-2.357, 0.048)
14	33.544	(-2.218, -0.024)
14.5	33.334	(-2.148, -0.024)

Table 4: Reference time averaged helium volume fraction  $\langle X_1 \rangle_t$  in horizontal  $xy$ -planes at different heights  $z$  covering the entire cavity: maximal values in % and their corresponding spatial  $(x, y)$  coordinates.

### Velocity distribution

Regarding the reference values of the velocity field, we present in figures 20 and 21 several horizontal and span-wise profiles respectively for the time averaged horizontal velocity component  $\langle u_1 \rangle_t$  and vertical velocity component  $\langle u_3 \rangle_t$ . The profiles are considered at the different heights covering the entire cavity, similarly at same positions of those considered previously for the helium field.

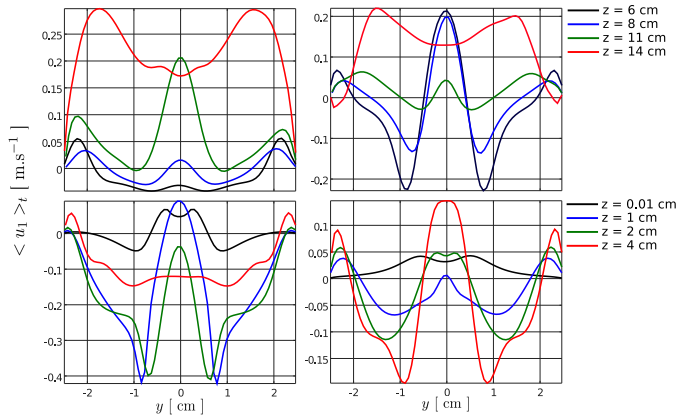


Figure 20: Span-wise time averaged horizontal velocity component  $\langle u_1 \rangle_t$  profiles at heights  $z = 0.01, 1, 2, 4$  cm (bottom series) and  $z = 6, 8, 11, 14$  cm (top series). Left top-bottom pair:  $x = -0.5$  cm, right top-bottom pair:  $x = -2$  cm.

Again, the almost symmetrical distribution is observed for all velocity components in the vertical planes parallel to the vents. In the mid-vertical  $xz$ -plane (left top-bottom pairs), the velocities distributions are directly dependent on the considered spatial positions and the dynamics that take place there.

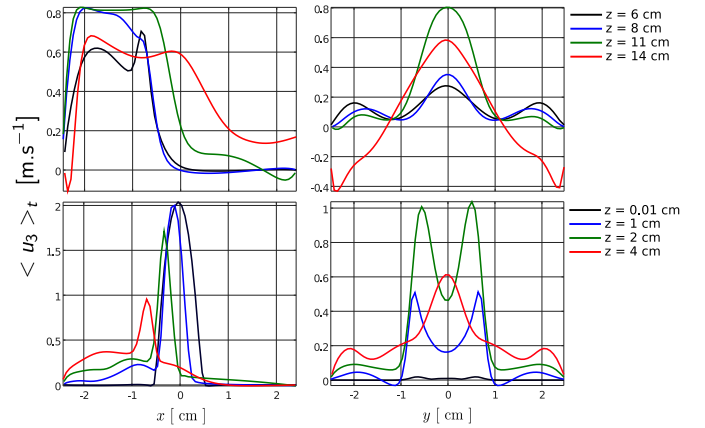


Figure 21: Horizontal and span-wise time averaged vertical velocity component  $\langle u_3 \rangle_t$  profiles at heights  $z = 0.01, 1, 2, 4$  cm (bottom series) and  $z = 6, 8, 11, 14$  cm (top series). Left top-bottom pair:  $x = -0.5$  cm, right top-bottom pair:  $x = 0$  cm.

For completeness, we present in tables 5, 6 and 7 the maximal/minimal values and their corresponding  $(x, y)$  coordinates in the same horizontal  $xy$ -planes considered before.

In a big portion of the cavity, the maximal  $\langle u_1 \rangle_t$  values are situated in the vicinity of the mid-vertical  $xz$ -plane ( $y = 0$ ) due to the entrainment phenomenon of the ambient with the inclined buoyant-jet axis. Similarly are the minimal values from the left side leading to the deformation of the axis (cross-flow).

Regarding the upward/downward convective flow, we note that the significant minimal values of  $\langle u_3 \rangle_t$  are more significant in the upper part of the cavity. This is rather expected as far as the negative velocities are generated from the top-ceiling

Height $z$ [cm]	Horizontal velocity component $\langle u_1 \rangle_t (x, y, z)$			
	Maximum value in the $xy$ -plane [ $\text{m.s}^{-1}$ ]	Location $(x, y)$ [cm]	Minimum value in the $xy$ -plane [ $\text{m.s}^{-1}$ ]	Location $(x, y)$ [cm]
1	0.261	(-0.964, -0.024)	-0.428	(-0.825, 0.822)
2	0.26	(-1.243, -0.024)	-0.429	(-1.034, -0.868)
3	0.255	(-1.452, -0.024)	-0.421	(-1.312, 0.891)
4	0.282	(-1.591, -0.024)	-0.398	(-1.452, 0.891)
5	0.310	(-1.591, -0.024)	-0.357	(-1.591, 0.891)
6	0.341	(-1.661, -0.024)	-0.298	(-1.661, 0.822)
7	0.362	(-1.591, -0.024)	-0.241	(-1.661, 0.822)
8	0.362	(-1.521, -0.024)	-0.183	(-1.591, 0.753)
9	0.341	(-1.382, -0.024)	-0.127	(-1.521, 0.753)
10	0.308	(-1.243, -0.024)	-0.085	(-1.452, 0.753)
11	0.264	(-1.034, 0.048)	-0.046	(-1.382, 0.753)
12	0.223	(1.359, -1.626)	-0.043	(-2.218, -1.833)
13	0.336	(-1.243, 1.718)	-0.001	(-2.427, -2.385)
14	0.448	(2.404, -2.316)	-0.055	(-1.661, -2.385)
14.5	0.524	(2.404, -2.316)	-0.185	(-2.148, -0.868)

Table 5: Reference time averaged horizontal velocity component  $\langle u_1 \rangle_t$  in horizontal  $xy$ -planes at different heights  $z$  covering the entire cavity: maximal/minimal values in  $\text{m.s}^{-1}$  and their corresponding spatial  $(x, y)$  coordinates.

Height $z$ [cm]	Horizontal velocity component $\langle u_2 \rangle_t (x, y, z)$			
	Maximum value in the $xy$ -plane [ $\text{m.s}^{-1}$ ]	Location $(x, y)$ [cm]	Minimum value in the $xy$ -plane [ $\text{m.s}^{-1}$ ]	Location $(x, y)$ [cm]
1	0.244	(-1.313, -0.592)	-0.249	(-1.243, 0.546)
2	0.241	(-0.686, 0.546)	-0.240	(-0.686, -0.523)
3	0.243	(-0.895, 0.615)	-0.242	(-0.895, -0.592)
4	0.24	(-2.009, -0.592)	-0.242	(-2.009, 0.615)
5	0.255	(-2.079, -0.523)	-0.26	(-2.079, 0.546)
6	0.251	(-2.148, -0.452)	-0.257	(-2.148, 0.476)
7	0.218	(-2.148, -0.452)	-0.222	(-2.148, 0.476)
8	0.171	(-2.079, -0.452)	-0.174	(-2.079, 0.405)
9	0.133	(-1.87, -0.452)	-0.136	(-1.87, 0.476)
10	0.104	(-1.730, -0.452)	-0.109	(-1.73, 0.405)
11	0.085	(2.195, -0.73)	-0.082	(-1.521, 0.405)
12	0.225	(0.941, -1.557)	-0.193	(1.22, 1.511)
13	0.177	(-1.313, -1.971)	-0.167	(-1.173, 1.994)
14	0.272	(-2.079, 1.374)	-0.286	(-2.079, -1.282)
14.5	0.493	(-0.333, 1.443)	-0.497	(-0.333, -1.489)

Table 6: Reference time averaged span-wise velocity component  $\langle u_2 \rangle_t$  in horizontal  $xy$ -planes at different heights  $z$  covering the entire cavity: maximal/minimal values in  $\text{m.s}^{-1}$  and their corresponding spatial  $(x, y)$  coordinates.

impact that creates the vortices and the recirculations at the top of the cavity.

## References

- [1] BR Morton, GI Taylor, and JS Turner. Turbulent gravitational convection from maintained and instantaneous sources. *Proceedings of the Royal Society of London. Series A. Mathematical and Physical Sciences*, 234 (1196):1–23, 1956.

Height $z$ [cm]	Horizontal velocity component $\langle u_3 \rangle_t (x, y, z)$			
	Maximum value in the $xy$ -plane [ $\text{m}\cdot\text{s}^{-1}$ ]	Location $(x, y)$ [cm]	Minimum value in the $xy$ -plane [ $\text{m}\cdot\text{s}^{-1}$ ]	Location $(x, y)$ [cm]
1	2.001	(-0.119, 0.048)	-0.033	(-0.476, 1.098)
2	1.713	(-0.333, 0.048)	-0.012	(2.404, -1.971)
3	1.21	(-0.546, 0.119)	-0.014	(2.264, -2.109)
4	0.957	(-0.686, 0.119)	-0.018	(1.359, -1.351)
5	0.808	(-0.755, 0.048)	-0.021	(1.359, 1.649)
6	0.84	(-2.148, 0.546)	-0.023	(1.289, 1.718)
7	0.836	(-2.218, 0.546)	-0.022	(1.08, -1.971)
8	0.825	(-1.939, 0.048)	-0.022	(0.663, -2.109)
9	0.843	(-1.243, 0.333)	-0.029	(0.167, -2.247)
10	0.84	(-1.104, 0.262)	-0.077	(2.125, 0.048)
11	0.828	(-2.009, -0.024)	-0.109	(2.265, -1.282)
12	0.813	(-2.009, -0.024)	-0.233	(0.941, -1.902)
13	0.782	(-2.009, -0.024)	-0.519	(0.381, -2.247)
14	0.688	(-1.87, -0.024)	-0.456	(-0.048, -2.316)
14.5	0.552	(-1.939, -0.024)	-0.505	(-2.357, -0.024)

Table 7: Reference time averaged vertical velocity component  $\langle u_3 \rangle_t$  in horizontal  $xy$ -planes at different heights  $z$  covering the entire cavity: maximal/minimal values in  $\text{m}\cdot\text{s}^{-1}$  and their corresponding spatial  $(x, y)$  coordinates.

- [2] B Fuster, D Houssin-Agbomson, S Jallais, E Vyazmina, G Dang-Nhu, G Bernard-Michel, M Kuznetsov, V Molkov, B Chernyavskiy, V Shentsov, et al. Guidelines and recommendations for indoor use of fuel cells and hydrogen systems. *International Journal of Hydrogen Energy*, 42(11):7600–7607, 2017.
- [3] G Bernard-Michel and D Houssin-Agbomson. Comparison of helium and hydrogen releases in 1 m 3 and 2 m 3 two vents enclosures: Concentration measurements at different flow rates and for two diameters of injection nozzle. *International Journal of Hydrogen Energy*, 42(11):7542–7550, 2017.
- [4] JS Turner. Buoyant plumes and thermals. *Annual Review of Fluid Mechanics*, 1(1):29–44, 1969.
- [5] CJ Chen and W Rodi. Vertical turbulent buoyant jets: a review of experimental data. *NASA STI/Recon Technical Report A*, 80, 1980.
- [6] W Rodi. *Turbulent buoyant jets and plumes*, volume 3. Pergamon press Oxford, 1982.
- [7] B Cariteau and I Tkatschenko. Experimental study of the concentration build-up regimes in an enclosure without ventilation. *International Journal of Hydrogen Energy*, 37(22):17400–17408, 2012.
- [8] PF Linden, GK Batchelor, HK Moffatt, and MG Worster. Convection in the environment. *Perspectives in Fluid Dynamics: A Collective Introduction to Current Research*, pages 289–345, 2000.
- [9] G Abraham. Entrainment principle and its restrictions to solve problems of jets. *Journal of Hydraulic Research*, 3(2):1–23, 1965.
- [10] EJ List and J Imberger. Turbulent entrainment in buoyant jets and plumes. *Journal of the Hydraulics Division*, 99(9):1461–1474, 1973.
- [11] PF Linden, GF Lane-Serff, and DA Smeed. Emptying filling boxes: the fluid mechanics of natural ventilation. *Journal of Fluid Mechanics*, 212: 309–335, 1990.
- [12] PF Linden. The fluid mechanics of natural ventilation. *Annual Review of Fluid Mechanics*, 31(1):201–238, 1999.
- [13] WD Baines and JS Turner. Turbulent buoyant convection from a source in a confined region. *Journal of Fluid Mechanics*, 37(01):51–80, 1969.
- [14] Y.J.P. Lin and C.L. Lin. A study on flow stratification in a space using displacement ventilation. *Int. J. Heat and Mass Transfer*, 73:67–75, 2014.
- [15] O. Auban, F. Lemoine, P. Vallette, and J.R. Fontaine. Simulation by solutal convection of a thermal plume in a confined stratified environment: application to displacement ventilation. *Int. J. Heat and Mass Transfer*, 44:4679–4691, 2001.
- [16] GR Hunt and JM Holford. The discharge coefficient—experimental measurement of a dependence on density contrast. In *Proc. 21st AIVC Conference, The Hague, Netherlands*, 2000.
- [17] JM Holford and GR Hunt. The dependence of the discharge coefficient on density contrast—experimental measurements. In *Proceedings 14th Australasian Fluid Mechanics Conference (ed. BB Dally)*, pages 123–126, 2001.
- [18] O Vauquelin, EM Koutaiba, E Blanchard, and P Fromy. The discharge plume parameter and its implications for an emptying–filling box. *Journal of Fluid Mechanics*, 817:171–182, 2017.
- [19] G Desrayaud, E Chénier, A Joulin, A Bastide, B Brangeon, JP Caltagirone, Y Cherif, R Eymard, C Garnier, S Giroux-Julien, et al. Benchmark solutions for natural convection flows in vertical channels submitted to different open boundary conditions. *International Journal of Thermal Sciences*, 72:18–33, 2013.
- [20] E Saikali, G Bernard-Michel, A Sergent, C Tenaud, and R Salem. Highly resolved large eddy simulations of a binary mixture flow in a cavity with two vents: Influence of the computational domain. *International Journal of Hydrogen Energy*, 44(17):8856 – 8873, 2019.
- [21] G Bernard-Michel, E Saikali, and D Houssin. Experimental measurements, cfd simulations and model for a helium release in a two vents enclosure. In *Proceeding of the International Conference on Hydrogen Safety, Hamburg, Germany*, 2017.
- [22] E Saikali. *Numerical modelling of an air-helium buoyant jet in a two vented enclosure*. PhD thesis, Sorbonne Université, 2018.
- [23] G Bernard-Michel, E Saikali, A Sergent, and C Tenaud. Comparisons of experimental measurements and large eddy simulations for a helium release in a two vents enclosure. *International Journal of Hydrogen Energy*, 44(17):8935 – 8953, 2019.
- [24] FA Williams. *Combustion Theory*. Addison-Wesley series in engineering sciences. Addison-Wesley Publishing Company, 1965.
- [25] B Müller. Low-mach-number asymptotics of the navier-stokes equations. In *Floating, Flowing, Flying*, pages 97–109. Springer, 1998.
- [26] CR Wilke. A viscosity equation for gas mixtures. *The Journal of Chemical Physics*, 18(4):517–519, 1950.
- [27] DEN-CEA. Triocfd, <http://trio CFD.cea.fr/>.
- [28] A Wambecq. Rational runge-kutta methods for solving systems of ordi-

- nary differential equations. *Computing*, 20(4):333–342, 1978.
- [29] Y Saad. *Iterative methods for sparse linear systems*. SIAM, 2003.
- [30] K Mahesh. The interaction of jets with crossflow. *Annual Review of Fluid Mechanics*, 45:379–407, 2013.
- [31] P Chassaing, RA Antonia, F Anselmet, L Joly, and S Sarkar. *Variable density fluid turbulence*, volume 69. Springer Science & Business Media, 2013.
- [32] F Plourde, MV Pham, SD Kim, and S Balachandar. Direct numerical simulations of a rapidly expanding thermal plume: structure and entrainment interaction. *Journal of Fluid Mechanics*, 604:99–123, 2008.
- [33] G. Carazzo, E. Kaminski, and S. Tait. The route to self-similarity in turbulent jets and plumes. *Journal of Fluid Mechanics*, 547:137–148, 2006.